



Retrospective and Recent Examples of Aircraft and Rotorcraft System Identification at DLR

Christoph Deiler,^{*} Wulf Mönnich,[†] Susanne Seher-Weiß,[‡] and Johannes Wartmann[‡]
DLR, German Aerospace Center Braunschweig, Germany

<https://doi.org/10.2514/1.C037262>

Aircraft system identification has a five-decades-long tradition at German Aerospace Center (DLR). Over the last two decades, the research covered various topics related to system identification of fixed- and rotary-wing aircraft, nonconventional applications and atmospheric effects, the development of new flight-test procedures for system identification purposes, and specific aircraft model enhancements and corresponding parameter estimation. Comprehensive tools were developed that support this research and can be applied to a variety of different problems and types of vehicles. The paper starts with a short description of the different system identification methods used at DLR and the corresponding tools. The discussion of flight-test procedures and maneuver design as well as sensor fusion and flight-path reconstruction provides information on how to optimize the flight tests for system identification and to arrive at a consistent flight-test database. The examples for fixed-wing aircraft provide information on identification including abnormal conditions such as icing and interaction with atmospheric disturbances as well as modeling of structural mechanics and loads. The identification of high-order rotorcraft models that account for rotor and engine dynamics and even structural modes is discussed, and the identification of rotor mast moments as well as the identification of non-physics-based models and their integration into physics-based models are also covered. A final section shows that system identification can also be used to derive models for gyroplanes and parachutes as well as to derive control equivalent turbulence input models and to estimate complex wind field geometries. Thus, a broad overview of possible applications of system identification is given.

I. Introduction

AIRCRAFT and rotorcraft flight dynamics simulation models require high levels of fidelity to be suitable as prime items in support of life cycle practices, particularly vehicle and control design and development, and system and trainer certification. Modern system identification methods have been developed in recent years [1–3] that provide new approaches well suited to pilot-in-the-loop fidelity assessment and systematic techniques for updating simulation models to achieve the needed level of fidelity. A broad overview of applying system identification to aircraft and rotorcraft was given in the past in Refs. [4,5]. More recently, the use of system identification for improving the fidelity of rotorcraft flight simulation models was described in Ref. [6].

At DLR, German Aerospace Center (DLR), accurate aircraft and rotorcraft models are needed for dynamic simulation, flight control system development, and handling qualities evaluations. These applications demand advanced models and high-fidelity aerodynamic databases of flight vehicles. System identification is extensively and routinely used to meet these challenging demands by generating validated models and databases from flight data. An overview of system identification applications at DLR was given in Ref. [7] and is continued with this paper.

During the last decades, models for several different fixed-wing aircraft were identified. Driven by DLR's acquisition of the Airbus A 320 research aircraft Advanced Technology Research Aircraft (ATRA) (see Fig. 1), a corresponding simulation model for, for example, simulator training, flight dynamics analysis, and development of novel pilot assistance functions or innovative controller

design was developed using flight-test data from several extensive flight-test campaigns. In cooperation with the Brazilian manufacturer Embraer, models for a Phenom 300 business jet and the Embraer E 190-E2 were identified from flight-test data, including special conditions like icing or model extensions for including structural dynamics in the models. Additional system identification work was performed for, for example, a Remos GX single-engine airplane and different gyroplanes. The latest addition to DLR's aircraft fleet is a Dassault Falcon 2000 LX named In-Flight Systems and Technologies Airborne Research for which two flight-test campaigns in 2022 delivered the first data for system identification.

On the rotorcraft side, DLR operates the Active Control Technology/Flying Helicopter Simulator (ACT/FHS) (see Fig. 2) as a test bed for various research projects; see, for example, Refs. [8–10]. The ACT/FHS is based on an Airbus Helicopters H135, a light, twin-engine helicopter with a bearingless main rotor and a fenestron, and features a highly modified flight control system [11]. Models of different complexity for the ACT/FHS are needed for simulation and flight control law development.

The unique test vehicles are complemented by the Air Vehicle Simulator (AVES) facility located in Braunschweig, which features a fixed-base and a motion-base simulator with interchangeable Airbus A320 and Airbus Helicopters H135 cockpits [12].

The paper starts with a short description of the system identification methods and corresponding software tools that were developed and are routinely used at DLR. Next, the different aspects of generating a consolidated flight-test database are discussed. The section on fixed-wing models covers the modeling and identification of novel aircraft configurations, structural dynamics, and loads as well as specific aspects such as icing. The section on rotorcraft identification deals with the modeling of the various rotor degrees of freedom, engine dynamics, and generating a wide-envelope model by combining linear models derived at different flight conditions. The application of system identification to other types of aircraft such as gyrocopters or parachutes, the modeling of turbulence, and the prediction of wind fields is covered in a final section.

II. Identification Methods and Software Tools

A. Methods

Three identification methods are routinely used at DLR: 1) the maximum likelihood (ML) output error method, 2) the frequency

Received 25 October 2022; revision received 22 February 2023; accepted for publication 26 March 2023; published online Open Access 7 June 2023. Copyright © 2023 by Deutsches Zentrum fuer Luft- und Raumfahrt e.V. (DLR). Published by the American Institute of Aeronautics and Astronautics, Inc., with permission. All requests for copying and permission to reprint should be submitted to CCC at www.copyright.com; employ the eISSN 1533-3868 to initiate your request. See also AIAA Rights and Permissions www.aiaa.org/randp.

*Research Engineer, Institute of Flight Systems, Department of Flight Dynamics and Simulation.

[†]Scientific Advisor, Institute of Flight Systems, Department of Flight Dynamics and Simulation.

[‡]Research Engineer, Institute of Flight Systems, Rotorcraft Department.



Fig. 1 DLR's Airbus A 320 research aircraft ATRA.



Fig. 2 DLR's research helicopter ACT/FHS.

response (FR) method, 3) the optimized predictor-based subspace identification (PBSIDopt) method. For the classical methods ML and FR, a model structure has to be specified, which is usually derived from physical considerations. Then, the model parameters are estimated based on a given cost function. For the PBSIDopt method, only the model order and two integer parameters have to be specified. The model structure and corresponding parameters are estimated automatically by the algorithm. All three methods are described in the next subsections.

1. Maximum Likelihood Output Error Method

The system to be identified is assumed to be described by a continuous-time state-space model,

$$\begin{aligned}\dot{\mathbf{x}}(t) &= f(\mathbf{x}(t), \mathbf{u}(t), \boldsymbol{\theta}) \\ \mathbf{y}(t) &= g(\mathbf{x}(t), \mathbf{u}(t), \boldsymbol{\theta})\end{aligned}\quad (1)$$

where \mathbf{x} denotes the state vector, \mathbf{u} denotes the input vector, and \mathbf{y} denotes the output vector. The unknown model parameters are denoted by $\boldsymbol{\theta}$. Measurements \mathbf{z} of the outputs exist for N discrete time points t_k :

$$\mathbf{z}_k = \mathbf{y}(t_k) + \mathbf{v}(t_k), \quad k = 1, \dots, N \quad (2)$$

The measurement noise \mathbf{v} is assumed to be characterized by Gaussian white noise with covariance matrix \mathbf{R} .

The ML estimates of the unknown parameters $\boldsymbol{\theta}$ are obtained by minimizing the cost function

$$\begin{aligned}J(\boldsymbol{\Theta}, \mathbf{R}) &= \frac{1}{2} \sum_{k=1}^N [\mathbf{z}(t_k) - \mathbf{y}(t_k)]^T \mathbf{R}^{-1} \\ &\quad \times [\mathbf{z}(t_k) - \mathbf{y}(t_k)] + \frac{N}{2} \ln(\det(\mathbf{R}))\end{aligned}\quad (3)$$

The optimization of Eq. (3) is carried out in two steps. In the first step, it can be shown that for any given value of $\boldsymbol{\theta}$ the ML estimate of \mathbf{R} is given by

$$\mathbf{R} = \frac{1}{N} \sum_{k=1}^N [\mathbf{z}(t_k) - \mathbf{y}(t_k)][\mathbf{z}(t_k) - \mathbf{y}(t_k)]^T \quad (4)$$

Having obtained an estimate of \mathbf{R} , any optimization method can be applied to update the parameter vector $\boldsymbol{\theta}$.

For linear continuous-time state-space models

$$\begin{aligned}\dot{\mathbf{x}}(t) &= \mathbf{A}(\boldsymbol{\theta})\mathbf{x}(t) + \mathbf{B}(\boldsymbol{\theta})\mathbf{u}(t) \\ \mathbf{y}(t) &= \mathbf{C}(\boldsymbol{\theta})\mathbf{x}(t) + \mathbf{D}(\boldsymbol{\theta})\mathbf{u}(t)\end{aligned}\quad (5)$$

a frequency-domain variant of the ML methods exists where the measured data are first transformed into the frequency domain using a fast Fourier transform. This leads to a similar cost function as for the time-domain variant.

More details about the time- and frequency-domain variants of the ML method and their implementation at DLR can be found in Refs. [1,7,13].

2. Frequency Response Method

The ML method in the frequency domain is based on matching the Fourier transform of the output variables. In contrast, the FR method is based on matching the frequency responses, in other words, the ratio of the output per unit of control input as a function of control input frequency.

For the linear state-space system from Eq. (5), the frequency response matrix is determined as

$$\mathbf{T}(s) = \mathbf{C}(s\mathbf{I} - \mathbf{A})^{-1} \mathbf{B} + \mathbf{D} \quad (6)$$

where \mathbf{I} denotes the identity matrix.

The quadratic cost function to be minimized for the frequency response method is

$$\begin{aligned}J &= \frac{20}{N_\omega} \sum_{k=1}^{N_\omega} w_\gamma(k) [(|T_m(k)|_{dB} - |T(k)|_{dB})^2 \\ &\quad + w_{ap} (\Delta T_m(k) - \Delta T(k))^2]\end{aligned}\quad (7)$$

where T and T_m are a single frequency response and its measured counterpart, N_ω is the number of frequency points in the frequency interval $[\omega_1, \omega_{N_\omega}]$, $|\dots|_{dB}$ denotes the amplitude in decibels, $\Delta(\dots)$ is the phase angle in degree, and w_{ap} is the relative weight between amplitude and phase errors. The normal convention from Ref. [14] is $w_{ap} = 0.01745$.

The optional heuristic weighting function w_γ is based on the coherence between the input and the output at each frequency. It is defined as

$$w_\gamma(k) = [1.58(1 - e^{j\gamma_{xy}(k)})]^2 \quad (8)$$

This coherence weighting allows an emphasis to be placed on matching the frequency responses in those frequency ranges with the highest coherence and deweighting data with low coherence.

A good overview of system identification using the frequency response method is found in Ref. [2].

3. Predictor-Based Subspace Identification Method

The PBSIDopt method identifies a linear discrete-time state-space model,

$$\begin{aligned}\mathbf{x}_{k+1} &= \mathbf{A}_d \mathbf{x}_k + \mathbf{B}_d \mathbf{u}_k \\ \mathbf{y}_k &= \mathbf{C}_d \mathbf{x}_k + \mathbf{D}_d \mathbf{u}_k\end{aligned}\quad (9)$$

for N discrete data points $k = 1 \dots N$ in the time domain. PBSIDopt is, like other subspace methods, basically a two-step approach. In the first step, the system states are reconstructed from available input/output measurements. For this, the parameters of a high-order vector-autoregressive model with exogenous input (ARX) model of order p are estimated and then used to set up the extended observability matrix of rank $n_y \cdot f$ and f is a user (integer) parameter. A subsequent singular value decomposition of this matrix finally reconstructs the system states. In the second step, the system matrices of a linear discrete-time state-space model of order n are estimated from the inputs, outputs, and reconstructed states.

In both steps, only the model orders p and n as well as the integer parameter f have to be specified, but no model structure or initial values are required. The model order n determines the most significant model states which are selected by the algorithm. Additionally, p and f have a major influence on the accuracy of the identified models and their invariant characteristics like the model eigenvalues. An approach to choose n , p , and f can be found in Ref. [15]. PBSIDopt provides consistent estimates even when using noisy and correlated data from closed-loop experiments. The resulting models have fully populated system matrices and usually nonphysical states. However, the identified model can be transformed in such a way that the first n_y state variables correspond to the output variables by using the transformation described in Ref. [16]. Accuracy information for the model parameters themselves are not available, but model accuracy metrics for the invariants of the estimated models (such as eigenvalues or transfer functions) based on bootstrap approaches or the asymptotic variance can be estimated.

The PBSIDopt method was introduced and described in Refs. [17–19] and compared to other closed-loop subspace identification methods in Ref. [20]. More details about the PBSIDopt method including a complete description and examples for combining this blackbox method with the classical ML and FR methods can be found in Ref. [21] or in Secs. V.D and V.E of this paper.

B. Tools

Several software tools were developed at DLR to support the various system identification efforts.

1. FITLAB

FITLAB is an integrated software tool for data analysis, system identification, and rotorcraft handling qualities analysis that is written in MATLAB® and has a graphical user interface. The data analysis part allows for data preprocessing, frequency response generation, and data visualization of both time-domain and frequency-domain data.

The identification methods implemented in FITLAB are the ML output error method in both time and frequency domain and the FR method. The ML method in the time domain is available for both linear and arbitrary nonlinear models. The FR method can be used to identify polynomial transfer function models for single frequency responses or for the identification of linear models from a set of frequency responses. The minimization of the respective cost function is performed either with a Gauss–Newton or a simplex-based optimization method. Both optimization variants allow for specifying bounds for the unknown parameters.

An optional add-on to FITLAB allows for handling qualities (HQ) evaluation of rotorcraft. The HQ evaluation implements quantitative criteria like, for example, bandwidth, dynamic stability, and several coupling criteria. Furthermore, an automatic evaluation of various mission task element maneuvers from ADS-33 [22,23] is implemented. More details on FITLAB can be found in Ref. [13].

2. ESTIMA

With FITLAB becoming the standard system identification software at DLR during the last decade, the Fortran-77 software tool ESTIMA [24] was not further developed. Nevertheless, ESTIMA is still available, as it consists of high-performance algorithms and is optimized to process large-scale systems and huge amounts of measured data, which is an advantage compared to FITLAB. It includes

the required functions to solve a system identification problem in the time domain with an equation-error or output-error method.

3. Online System Identification Tools

A fast and reliable system identification during flight test can achieve a significant reduction of flight-test time, costs, and effort and therefore improve the overall model development process. Furthermore, if specific information about the aerodynamics and control capabilities of a novel aircraft is already available during the flight test, envelope expansion for further flight-test points would be much easier.

DLR has developed and tested two different tools based on different methodologies for online system identification. The Rapid Aerodynamic Parameter Identification Tool (RAPIT) software [25] uses the well-known Fourier transform regression method for identification of aerodynamic model parameters, previously developed by Morelli [26]. Initial tests during an extensive flight-test campaign with DLR's research aircraft ATRA show very good and reliable results for the parameter estimates.

A second approach developed by DLR is an integrated identification loop consisting of a data selection tool and a time-domain parameter estimation tool [27]. This tool can consist of a specific implementation of ESTIMA or FITLAB, depending on the model language (FORTRAN, C/C++ or MATLAB®/Simulink) requirements.

Both tools further demonstrated their capabilities of successful flight-test support during high-risk icing flights where the online system identification results were required to continuously monitor the test aircraft's performance and control characteristics [28].

4. Virtual Flight-Test Data

To provide representative flight dynamics, the virtual test aircraft (VIRTTAC) model family was created starting in 2018. The first model, which is freely available for download on GitHub,⁴ is a short-to medium-range airliner named VIRTTAC-Castor [29]. The VIRTTAC models are meant to put the user virtually (through simulation) in the position of a flight-test engineer who is confronted with a new aircraft and performing flight tests. One possible application is the generation of a suitable database for system identification purposes as given in Ref. [30].

III. Generation of Consolidated Flight-Test Data

System identification is based on flight-test data from the vehicle to be modeled. When generating these data, care has to be taken that the vehicle is sufficiently excited. Depending on the vehicle and the chosen identification method, different types of excitation or maneuvers are suitable. Once the flight tests have been performed, data from different sensors have to be combined, and the consistency of the generated data has to be checked.

A. Flight-Test Procedures/Maneuver Design

For the classical ML and FR identification methods from Secs. II.A.1 and II.A.2, special maneuvers are usually performed to arrive at a suitable database. For time-domain identification, as mostly used for fixed-wing applications, multistep inputs are preferred. Rotorcraft identification is mostly performed with frequency-domain methods, and frequency sweep inputs in all controls are used as maneuvers. All maneuvers for system identification are preferably performed open loop to avoid correlation between the different control surfaces. Maneuvers with dissimilar control inputs should be used for validation purposes.

1. Design of Novel Maneuver Inputs for More Efficient System Identification

Classical maneuvers for system identification are mostly one-surface-at-a-time inputs and need to be performed several times at each flight condition. To overcome these restrictions, various methods for defining very information-rich multi-axis maneuvers already exist and have proven their efficiency, for example, maneuvers based on multisines/sum of sines signals [3]. DLR recently developed a new

⁴See <https://github.com/VIRTTAC/VIRTTAC> [retrieved 26 March 2023].

design method based on the wavelet transform allowing the definition of multi-axis inputs in the time-frequency domain [31,32]. The goal of this research approach was to propose new ways to design maneuvers, which can, furthermore, be used to reduce flight-test time or improve the accuracy of airplane simulation models. The proposed method allows designing multi-axis excitation maneuvers by specifying the frequency content and the corresponding timeframes when the frequencies are excited. When flight testing an aircraft, the dynamic characteristics are not exactly known *a priori* but predicted to be close to certain frequencies. Using the proposed technique of signal design, the aircraft can be excited with a certain frequency bandwidth around that prediction at a certain time during the maneuver. With one dedicated and relatively short maneuver, the aircraft motion can be excited at and around all relevant frequencies in all axes. This would reduce the need for repeating classical maneuvers with a wide-range frequency excitation and might merge the advantages of these with the multisines approach using only a certain set of discrete frequencies.

The method's basic idea uses the fact that a wavelet transform yields a time-frequency representation (TFR) of a signal and that the signal can be reconstructed from its TFR. Starting by specifying the desired TFR, the designed input signals can be generated by an inverse wavelet transform. Hence, the parameterization of the input signal definition is performed by using only a few parameters to define the correlation between time and frequency in the time-frequency plane (TFP). An explicit explanation of the wavelet transform and its applications to input signal design can be found, for example, in Refs. [27,32,33].

An overview of the methodology is given in Fig. 3. Aircraft *a priori* information can be used to select the desired frequency bands for the signal. Heisenberg boxes in the TFP are used to represent this information in the time/frequency domain. An inverse discrete wavelet packet transform using a selected wavelet yields the desired signal in the time domain, which can then be assigned to any of the control surfaces.

As an example, an elevator signal generation is shown in Fig. 4. The top plot gives the definition of the 32×16 TFP, which results in Heisenberg boxes with a width of 2 s and a height of approximately 0.2753 Hz. The time history plot in the middle shows the resulting signal from the inverse wavelet packet transform. The bottom plot provides the resulting elevator signal's frequency content. As defined, no frequency above 2 Hz is included to ensure only exciting the aircraft's rigid-body dynamic modes. A much more detailed analysis of the input signals, the corresponding model identification, and a discussion of the results is given in Ref. [32].

All in all, the proposed methodology allows the user to design complex signals both with and without *a priori* information of the

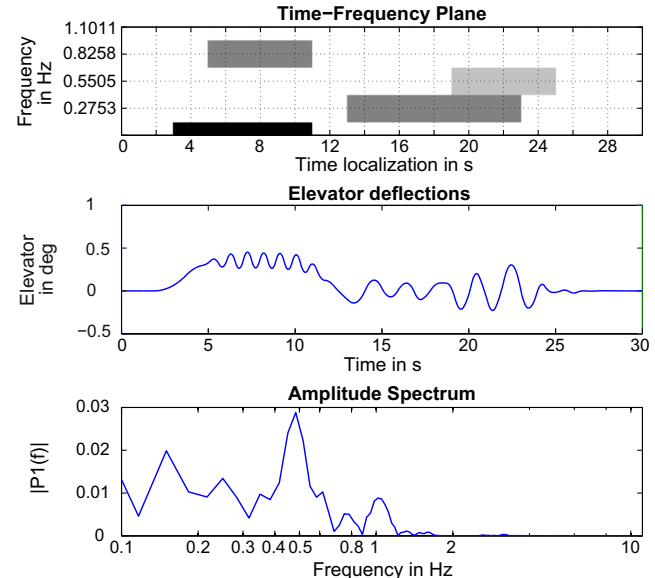


Fig. 4 Example of elevator signal generation: time/frequency plane (top), generated signal time history (middle), and amplitude spectrum (bottom). Grayscale in TFP indicates different wavelet coefficient values. Adapted from Ref. [32].

system to be identified. Moreover, only a quite restricted number of parameters is required to define these input signals.

Another approach to multi-axis maneuver design is to use the method proposed in Ref. [34], which uses genetic algorithms to optimize the power spectra for multi-axis multisine inputs or to define the switching times for multi-axis multistep inputs, based on cost functions computed from the information matrix associated with a known design model.

2. Generalized Binary Noise for Closed-Loop Rotorcraft System Identification

As mentioned previously, common rotorcraft system identification approaches use frequency sweeps for each control input and flight condition. Flying frequency sweeps require a trained test pilot simultaneously applying the required control input, stabilizing the rotorcraft, and maintaining a flight state near the reference trim. Therefore, these flight tests are challenging, require extensive pilot and crew training, and often result in very time- and cost-intensive flights but also in excellent open-loop frequency responses. A flight control

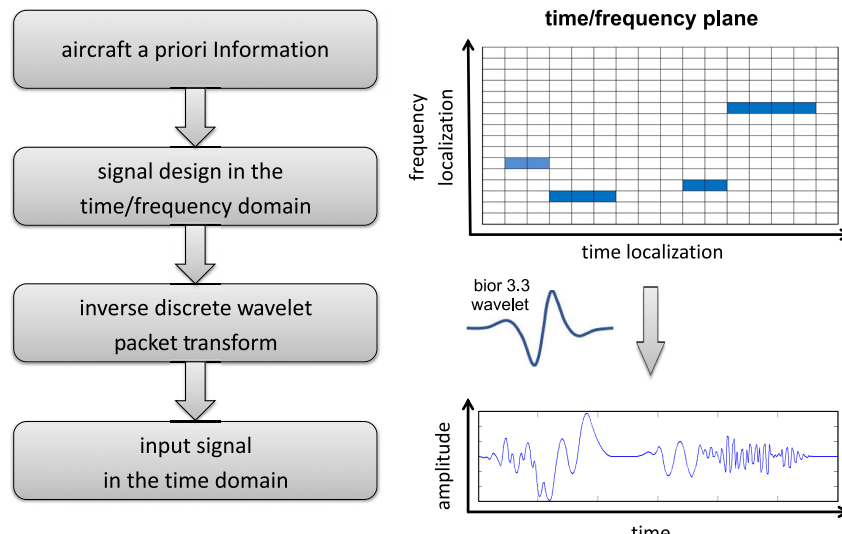


Fig. 3 Overview of proposed maneuver design method based on the idea of creating input signals with distinct frequency band excitations at predefined times, adapted from Ref. [32].

system can considerably ease this task (see Ref. [2], chapter 9), but frequency sweeps from closed-loop systems with highly or fully correlated control inputs require more-extensive postprocessing steps to reconstruct the correct open-loop frequency [35]. Orthogonal multisine inputs have been shown to be an alternative for multi-axis system identification, but an *a priori* optimization step is required to ensure small amplitudes [36]. Nonetheless, if *a priori* knowledge of the vehicle dynamics is available, suitable chosen multisines can be optimal test inputs.

Advanced test inputs are rarely used in industrial applications because complex input generators and/or laborious flight tests shall be avoided. More frequently, pseudorandom binary sequences ([PRBS] or pseudorandom binary noise) are applied for system identification in open- and closed-loop operations. PRBS has an almost white frequency spectrum and nearly evenly distributed energy and thus a smaller average amplitude than multisine waves. Generalized binary noise (GBN) as described in Ref. [37] is related to PRBS. In contrast to PRBS, GBN offers an adjustable frequency spectrum, which allows one to distribute the control energy nearly evenly over the frequency range of interest. Therefore, the average amplitude of such signals can be smaller in comparison to signals consisting of a small number of frequencies [38].

GBN has a smooth spectrum in the given frequency range and does not require *a priori* optimization. It can be implemented easily in a signal generator because only a random number generator and a switching logic is needed. Additionally, GBN shows advantages using a one-step-ahead prediction method like PBSIDopt; see Sec II.A.3. Nonetheless, random noise inputs like GBN can result in high control rates, and (randomly) pairwise signal correlations require adequate noise generators.

In Ref. [39], an industrially attractive closed-loop system identification approach is proposed and evaluated for multi-axis GBN excitation of the ACT/FHS rotorcraft simulation. Figure 5 shows the simplified closed-loop system of the ACT/FHS which consists of the feedback controller G_{FB} , the plant model G_M and two excitation signals r_1 (control system reference values, Ref) and r_2 (additional actuator controls, Ctr). Output noise is denoted as e , and the rotorcraft actuator inputs are denoted as u .

To ensure a persistent excitation of the full frequency range of interest, eight different GBN signals are needed for the ACT/FHS: four control system reference values (r_1 , Ref) for lower frequencies and four additive actuator signals (r_2 , Ctr) for mid and high frequencies. The total actuator commands $u = (\delta_{\text{lon}}, \delta_{\text{lat}}, \delta_{\text{ped}}, \delta_{\text{col}})$ of the ACT/FHS during a closed-loop system identification maneuver using GBN are shown in Fig. 6. The actuator command for longitudinal cyclic is denoted as δ_{lon} , lateral cyclic is denoted as δ_{lat} , pedal (tail rotor actuator) is denoted as δ_{ped} , and main rotor collective is denoted as δ_{col} . The resulting actuator amplitudes are small in comparison to conventional frequency sweeps, and all actuators are excited simultaneously. Additionally, the rotorcraft remains near the chosen trim point, because the flight control system is active.

In Ref. [39], different GBN frequency ranges for r_1 and r_2 are investigated, and the overall experiment time as well as the signal-to-noise ratio are compared to frequency sweeps. Accurate models of the open-loop bare airframe dynamics of the ACT/FHS could be identified using this closed-loop data applying the PBSIDopt system identification method, even though these maneuvers cannot be used for proper frequency response extraction [21].

B. Sensor Fusion and Flight-Path Reconstruction

Accurate vehicle states are needed among others for system identification and the later model validation step. In general, raw sensor

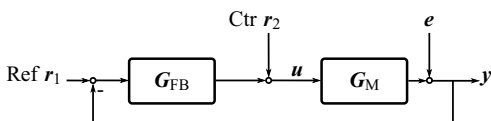


Fig. 5 Closed-loop system with excitation signals r_1 and r_2 , from Ref. [39].

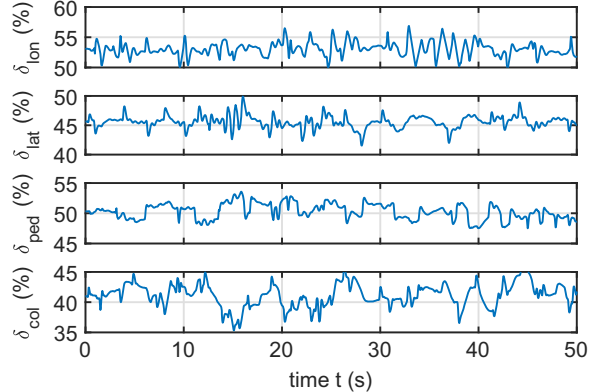


Fig. 6 Actuator commands during closed-loop system identification maneuver of the ACT/FHS, adapted from Ref. [39].

data cannot be used directly because, for example, sensor noise or bias can corrupt the system identification results. Thus, a postflight data processing step is required, which is often referred to as data consistency and compatibility check and state reconstruction; see Refs. [1,40] or [2]. Because the flown trajectory of the aircraft or rotorcraft is estimated in this procedure, this step is also called flight-path reconstruction (FPR) [41,42]. The aim of the FPR is to estimate the rotatory and translatory states of the vehicle and to possibly identify sensor models. In general, the six-degree-of-freedom rigid-body kinematics and a nonlinear observation model, for example, sensor models, are used to solve this state estimation problem.

For the FPR of the ACT/FHS, two unscented Kalman filters (UKF) [43] are used, because the aircraft kinematics and the observation model are nonlinear and UKFs showed improved performance over commonly used extended Kalman filters for highly nonlinear equations. Both UKFs are implemented as square-root unscented Kalman Filters [44] using a scaled unscented transform to improve numerical robustness [45]. To simplify the filter design and implementation, rotatory, translatory, and air data measurements are fused and filtered in two different filters: the rotatory and the FPR Kalman Filter. The structure of the overall rotorcraft FPR is shown in Fig. 7.

In the first module Rot, the different rotatory measurements y_{Rot} are corrected for sensor misalignment and then fused to x_{Rot} using the rotatory UKF. For the ACT/FHS, these rotatory measurements contain the rates and attitude angles from the two attitude and heading reference systems (AHRS) of the production aircraft and from a Honeywell inertial navigation system (INS). Separating the rotatory from the translatory states is possible because the rotatory states do not depend on translatory or air data measurements.

The estimated rotatory UKF states x_{Rot} are then used in the center of gravity module to transform the uncorrected translatory and air data measurements $y_{\text{FPR,uc}}$ to the rotorcraft's center of gravity (CG). In addition, x_{Rot} is used as an input in the FPR module, where the CG-corrected measurements y_{FPR} are used as measurements for the UKF update step. The translatory measurements comprise the translatory accelerations (of the two AHRS and the INS), the GPS position, and velocity (from the INS and one satellite-based augmented GPS). Airspeed, angle of attack, and angle of sideslip are used from the production rotorcraft air data sensors and the ACT/FHS's noseboom. The filter's measurement covariance depends on the current flight status; in other words, the airspeed-dependent measurement covariance of the air data sensors and the accuracy information provided by the GPS sensors are considered. Finally, the estimated states are processed by two separate unscented Rauch–Tung–Striebel smoothers (URTS) as described in Ref. [46]. Thus, the estimated states are smoothed in an optimal sense without an additional phase delay.

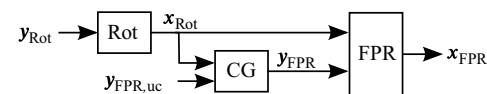


Fig. 7 Overall rotorcraft FPR module structure, from Ref. [46].

In addition to the FPR presented previously, an online FPR is implemented into the ACT/FHS to provide consistent data for the flight control system. The online FPR is implemented in the same manner except for the additional URTS smoothers. The offline and online flight-path reconstruction of the ACT/FHS is explained in detail in Ref. [47].

IV. Fixed-Wing Models

This section provides several descriptions of the work done at DLR besides the classical fixed-wing simulation model identification, highlighting specific research results and modeling/system identification approaches. Problems addressed herein reach from the analysis of operational flight data to the modeling of flexible aircraft.

A. Thrust Model Identification from Operational Flight Data

Aircraft operations are mainly driven by the vehicle's flight performance whose optimization is key to a sustainable future of aviation with fewer emissions. Therefore, high-quality simulation models of the actual flight performance, in other words, drag and thrust as functions of angle of attack, Mach number, static pressure, temperature, and so on, must be available for usage within the operation optimization process. There are several ways to obtain such models which are based on different sources of information about the distinct aircraft type. One very reliable source of information for these models are large operational flight databases, which then pose a big data problem. A smart way to solve such problems is the application of fundamental engineering knowledge together with well-established system identification techniques. Within these operational data, engine thrust and aircraft aerodynamics (especially the aircraft's drag) are directly correlated, which poses a challenge to any attempt to determine the desired flight performance models. The main assumption for the suggested approach is that big amounts of data allow one to decorrelate drag and thrust if the aerodynamics do vary due to flap/slat configuration changes and engine thrust is not dependent on these changes. It means that similar engine thrust conditions do exist for different aircraft configurations and consequently drag, which then allow one to determine each part (thrust and drag) individually.

The following iterative procedure was used to determine the lift/drag model and the engine thrust model from the operational data. First, a priori values for lift and drag for each flight condition and flap/slat configuration were calculated based on an assumed aircraft aerodynamics model (e.g., simple handbook-based formulation of aircraft drag polar and lift curve). Second, using this assumed aircraft drag, the required thrust to obtain a force equilibrium was calculated for each data point. Third, the engine thrust model was identified from the calculated required thrust data. Next, the aircraft lift and drag were recalculated based on measurements (inertial data and atmospheric parameters) and the output of the identified engine thrust model, and the parameters of the lift/drag model were estimated. If required, the corresponding model structure was identified in this step as well. Closing this loop allowed iterating until the aerodynamic model parameters had converged and the engine thrust model remained constant.

The thrust of a jet engine depends on several engine states and external parameters. Hence, the model formulation must cover the main influences to reliably predict the engine thrust within the required flight envelope and for all relevant thrust settings. The major parameters driving the jet engine thrust are given by engine fan speed N_1 , Mach number Ma , barometric altitude H , and temperature (in the given case, temperature offset from the standard atmosphere temperature ΔISA). In general, the engine thrust model is defined by

$$\begin{aligned} T &= T_{\text{net}} \cdot f_{\text{corr}}(\Delta ISA, \dots) \\ &= f(N_1, Ma, H) \cdot f_{\text{corr}}(\Delta ISA, \dots) \approx T_{\text{req}} \end{aligned} \quad (10)$$

where the required thrust T_{req} can be derived using the force balance in the aircraft longitudinal direction with the acceleration measurements and the (a priori) aerodynamics information. The model formulation contains two parts: the net thrust T_{net} formulation f depending on the fan speed, Mach number, and altitude and a temperature offset-

dependent correction f_{corr} . To obtain a suitable engine thrust model, the maximum likelihood problem

$$\hat{\boldsymbol{\theta}} = \arg \min_{\boldsymbol{\theta}} \left(\sum_{i=1}^N (z_i - y_i(\boldsymbol{\theta}))^2 \right) \quad (11)$$

must be solved, considering the required thrust as N measurements z and the thrust model output y . Different modeling approaches can be applied, resulting in different model accuracies and model determination efforts. The best model accuracy even outside the given data envelope can be achieved with a nonlinear thrust table model for T_{net} , which is able to represent the complex engine thrust behavior with the given regressors. The table is defined by a given number of breakpoints N_{BP} in each dimension and the thrust results from interpolation between the table entries. Hence, in the given case, the number of free parameters p for estimation is defined by

$$p = N_{\text{BP}_{N_1}} \cdot N_{\text{BP}_{Ma}} \cdot N_{\text{BP}_H}$$

One major requirement for the engine thrust table is that it should have a smooth shape and no significant local changes of curvature. No discontinuous behavior of thrust with fan speed, velocity or Mach number, and altitude or pressure should be expected. Furthermore, the fundamental engineering knowledge about jet engines and the way they produce thrust directly imposes the need to obtain *smooth* thrust curves; a jet engine within its normal operation limits will not produce an abrupt change of thrust due to a change of flight condition because the thermodynamic cycle within the engine is running continuously. As long as no major disturbance of this process occurs, like engine stall or any malfunction, there must be no significant change of thrust curvature with the used regressors. Without such assumptions, the resulting thrust model will not be able to reasonably and reliably predict the engine thrust. The optimization problem is reformulated as

$$\hat{\boldsymbol{\theta}} = \arg \min_{\boldsymbol{\theta}} \left(\sum_{i=1}^N (z_i - y_i(\boldsymbol{\theta}))^2 + \|\boldsymbol{\Gamma}_2^* \boldsymbol{\theta}\|^2 \right) \quad (12)$$

In this case, the Tikhonov regularization matrix $\boldsymbol{\Gamma}_2^*$ [48,49] is used to penalize the second-order derivatives of the multidimensional thrust table in each direction in order to smooth the table shape. The optimization problem in Eq. (12) can be solved by application of the iterative Gauss–Newton method.

As an example, Fig. 8 shows some results of the engine thrust table evaluation after identification. The results reflect the (steady) nonlinear engine thrust behavior. These results show that fundamental knowledge about the aircraft physics and smart application of system identification methods allow the reliable estimation of engine thrust models from a large database of operational flight data recordings.

Recent work on the identification of a nonlinear engine thrust model table for a large envelope is given in Refs. [50,51], and the reader is encouraged to consider these references for deeper insight into the work presented briefly herein.

B. Icing

Icing can have hazardous effects on aircraft performance characteristics and can be a limiting factor for the safe flight envelope. The change of the dynamic behavior and a potential premature stall raise the need for the pilot's situational awareness and an adaption of his/her control strategy. Aircraft icing again came more into focus of research after several serious accidents and the definition of new certification requirements for new transport aircraft for flight into icing conditions: Appendix O of CS-25 [52] or Federal Aviation Regulation (FAR) Part 25 [53]. These new requirements cover super-cooled large droplet (SLD) icing conditions and complement the existing requirements for icing conditions formulated in Appendix C of the regulations. In 2011, DLR started to develop novel model implementations to represent the icing effects on aircraft flight characteristics within several projects. The model formulations consist of a linear Δ -model approach to the already developed and identified clean (uniced) aircraft model. An arbitrary model parameter P including a

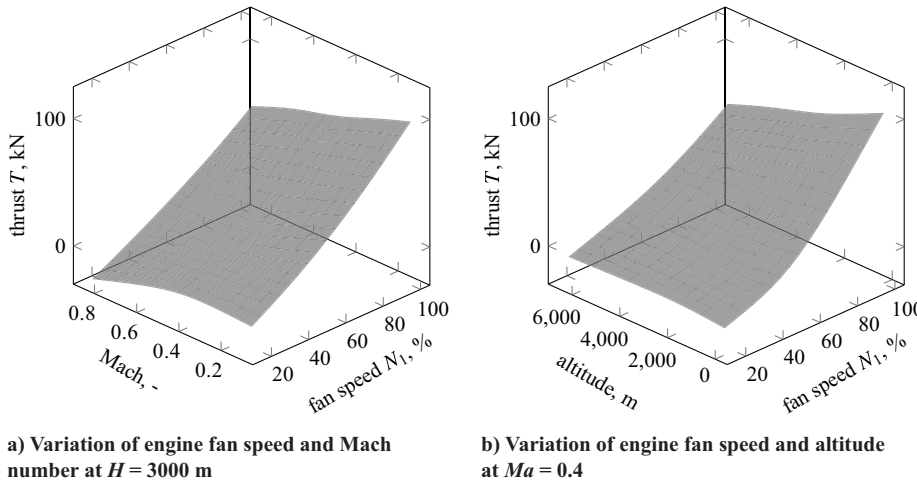


Fig. 8 Nonlinear thrust table evaluations at example conditions; example after identification from a large operational flight data set for a Pratt & Whitney PW1100G engine on an Airbus A 320neo. From Ref. [50].

basic model part P_{base} and an additional Δ -model part ΔP_{ice} can be expressed as

$$\begin{aligned} P &= (1 + k_P) \cdot P_{\text{base}} + d_P \\ &= P_{\text{base}} + \Delta P_{\text{ice}} \end{aligned} \quad (13)$$

Based on high-fidelity computational fluid dynamics simulations, an iced model for the well-known already retired DLR research aircraft Vereinigte Flugtechnische Werke (VFW) 614 Advanced Technologies Testing Aircraft System (ATTAS) including distributed icing effects on wings and the tailplane was formulated, identified, and analyzed [54,55]. Using an equation error approach, the Δ -model parameters were estimated for different ice configurations, resulting in a prediction of the icing-related changes in lift and drag coefficients as given in Fig. 9.

Furthermore, joint DLR/Embraer research on aircraft icing was established in 2012 and made a contribution to some of the key scientific aspects related to aircraft icing, for example, aircraft operational limitations and behavior with accumulated ice on various surfaces on the example of a Phenom 300 prototype. As an outcome of this research, various publications [55–59] present the major findings, the used modeling approach and identification results, and the analysis of the degrading effects of icing with regard to certain SLD ice configurations. During the development of the corresponding simulation models, new model formulations were derived and identified using an output error method in the time domain [56,57]. Figure 10 shows the lift and drag curves for the base aircraft and five different ice configurations, which could be extracted from the simulation models after identification. These results clearly revealed the different aerodynamic effects of specific ice configurations on the same aircraft, but they also show the mainly

degrading effects on flight performance. Proof-of-match plots illustrating the model quality after identification are given in Ref. [59]. Based on the system identification results and the obtained knowledge about the effects on aircraft icing, DLR developed a novel performance-based ice detection methodology [60], which only relies on standard aircraft avionics measurements and fundamental flight mechanics knowledge.

C. Structural Dynamics

The interest in accurately modeling flexible aircraft dynamics grew with the development of very large aircraft and the great research efforts toward the development of energy-efficient, environment-friendly aircraft, like solar-powered ones. The first structural modes of these configurations have lower natural frequencies than those of more conventional aircraft. But even for conventional aircraft, the future use of thin airfoils, high aspect ratios, and light materials will also shift the structural modes to lower natural frequencies, which will result in coupling with the rigid-body response. Hence, the classical split of (nearly) independent rigid-body (six-degree-of-freedom motion) flight mechanics and structural motion is not valid anymore.

To obtain the corresponding high-quality simulation models, DLR started a specific research project with a high-performance glider at the beginning of the last decade. Within this research, the applicability of system identification techniques in the time domain to include the effects of structural motion on an aircraft's classical flight dynamics was demonstrated. The SB 10 (Fig. 11), a high-performance two-seater glider designed and manufactured by Akaflieg Braunschweig, has a wingspan of 26 m and an aspect ratio of 31. Besides the classical control surfaces (elevator and rudder), the wing trailing edge has moving surfaces divided into three sections. The inner section is used as flaps, whereas the middle and outer portions act simultaneously as flaps or ailerons by symmetrical or antisymmetrical

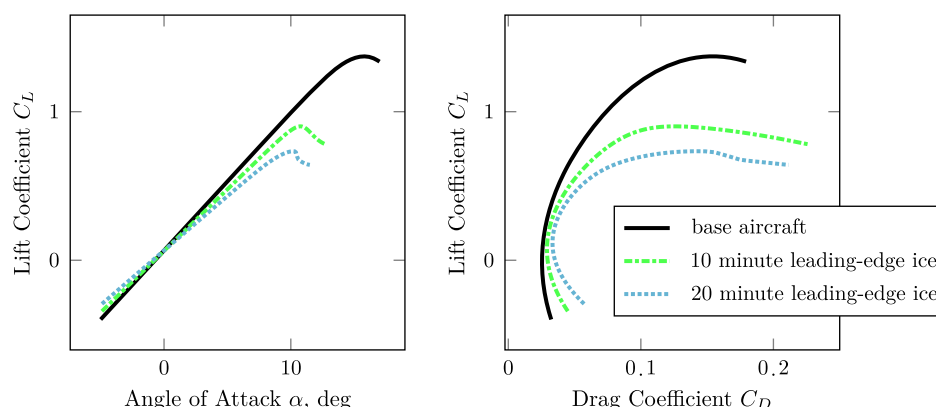


Fig. 9 Changes of lift and drag curves for different ice cases: 10 and 20 min ice accumulation at leading edge; aerodynamic model data for the VFW 614 ATTAS. From Ref. [55].

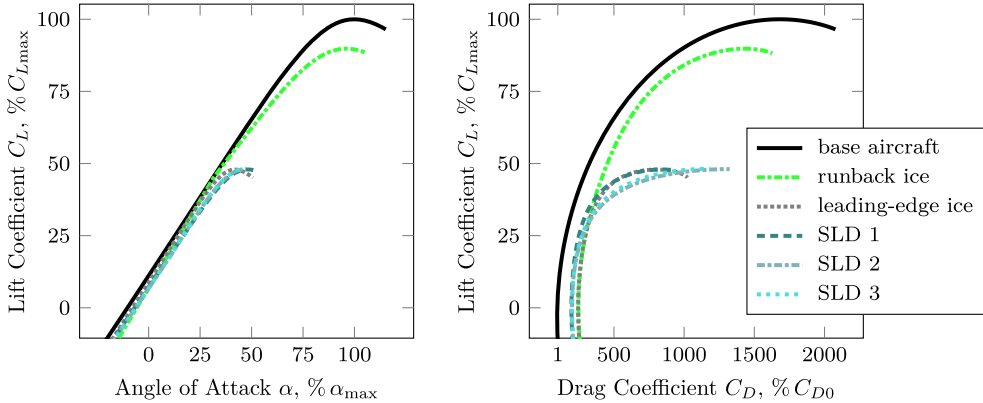


Fig. 10 Changes of lift and drag curves for different ice cases: leading-edge and runback ice (Appendix C of CS-25) and three SLD-ice configurations; aerodynamic model data (after identification) for the Phenom 300. Adapted from Ref. [59].

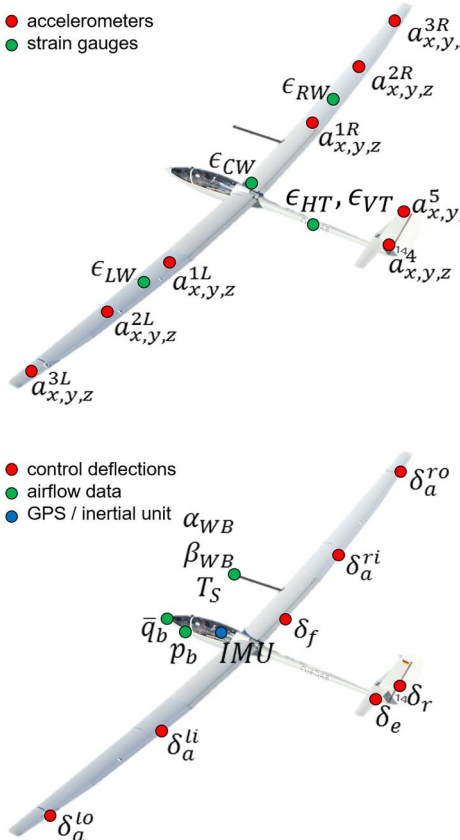


Fig. 11 Sensor locations on the SB 10 glider test aircraft: accelerometers a ; strain gauges ϵ ; control surface deflections δ ; airflow data $\alpha, \beta, \bar{q}, p, T_s$; inertial measurement unit (IMU) and GPS receiver. Adapted from Ref. [62].

deflection, respectively. The very high aspect ratio combined with the lightweight composite structure leads to high flexibility, with the first symmetric bending mode having a natural frequency of the order of 1 Hz. Such low frequencies allow the excitation of the structural modes by a human pilot deflecting the aircraft's control surfaces.

A test campaign was performed from the airport of Braunschweig, Germany, resulting in 11 flights with a total of 11 flight hours and 72 test points. The flight data consist of manually performed system identification maneuvers with, for example, (multi-)step inputs to ailerons, elevator, rudder, or flaps as well as sweep inputs for a broader frequency range of excitation.

In a data preprocessing step, additional signals like angular accelerations and low-pass-filtered angles of attack and sideslip were generated. The latter had to be filtered to remove the undesirable effects of vibrations of the wing boom. A comprehensive data compatibility check resulted in sensor models for, for example, the

angles of attack and sideslip, including, for example, the calibration factor, bias, and time delay. These steps provide a solid foundation for the subsequent identification of the flexible model.

In general, the modeling approach is based on the work of Waszak and Schmidt [61]. The equations of motion and the inertial decoupling between the rigid-body (R) and structural dynamics (F) are obtained through the use of the mean axes reference system.

The translational and rotational rigid-body equations of motion are given by

$$m(\dot{V}_b + \Omega_b \times V_b - T_{bg}g) = F_{\text{ext}} = F_R + F_F \quad (14)$$

$$I_b \dot{\Omega}_b + \Omega_b \times (I_b \Omega_b) = M_{\text{ext}} = M_R + M_F \quad (15)$$

where V_b, Ω_b are the vectors of translational speeds and rotational rates. I_b denotes the inertia tensor, and T_{bg} is the transformation matrix from geodetic to body-fixed reference system.

The dynamics equations for the N_f structural modes are given in generalized form,

$$\forall i \in [1, N_f], \quad \ddot{\eta}_i + 2\zeta_i \omega_i \dot{\eta}_i + \omega_i^2 \eta_i = \frac{Q_i}{m_i} = \frac{Q_{i,R} + Q_{i,F}}{m_i} \quad (16)$$

where η_i is the generalized displacement, ω_i is the mode frequency, ζ_i is the structural damping, and m_i is the generalized mass.

The external forces F_{ext} and moments M_{ext} driving the translational [Eq. (14)] and rotational [Eq. (15)] rigid-body equations of motion as well as the generalized moments Q_i driving the structural equations of motion [Eq. (16)] are composed of the sum of the aerodynamic forces, moments, or generalized moments due to the rigid-body response (including control deflection contributions) F_R , M_R , or $Q_{i,R}$, respectively, and forces or moments due to the flexible response F_F , M_F , or $Q_{i,F}$.

The structural displacement \mathbf{d} of an arbitrary point of the aircraft's structure is modeled as the sum of contributions from its normal modes represented by the generalized displacements and the mode shapes Φ :

$$\mathbf{d}(x, y, z, t) = \sum_i \Phi_i(x, y, z) \cdot \eta_i(t) \quad (17)$$

The aerodynamic forces F_R and moments M_R are represented by a derivative model formulation taking into account the major regressors for the classical aircraft aerodynamics, for example, angle of attack α ; angle of sideslip β ; true airspeed V_{TAS} ; control surface deflections δ ; or rotational rates p, q, r . The influence of the elastic modes on the external forces F_F and moments M_F is given through a coefficient model of the form

$$C_{(\cdot)F} = \sum_i C_{(\cdot)\eta_i} \cdot \eta_i + \sum_i C_{(\cdot)\dot{\eta}_i} \cdot \frac{\dot{\eta}_i \cdot l}{2 \cdot V_{\text{TAS}}} \quad (18)$$

where l denotes the reference length. Note that the forces and moments are calculated from the coefficients by multiplication with dynamic pressure and reference area, and reference length in case of moments.

The resulting expression for the influence of rigid-body motion and control surface deflections on the generalized loads $Q_{i,R}$ is given by a linear derivative model quite comparable to the aerodynamic model formulation accounting for the contributions of the angle of attack α ; angle of sideslip β ; control surface deflections δ ; and rotational rates p, q, r . The influence of modal deflections and velocities on the generalized loads $Q_{i,F}$ is defined by a coefficient model similar to Eq. (18).

The measurements of accelerometers \mathbf{a}^k distributed along the aircraft structure were used to reconstruct the elastic states and the shapes of the structural modes. The outputs of these sensors correspond to the sum of the accelerations \mathbf{a}^{CG} at the center of gravity, the inertial effects resulting from the distance between the sensor location and the center of gravity $\mathbf{r}^{CG,k}$, and the effects of structural motion,

$$\mathbf{a}^k = \mathbf{a}^{CG} + \dot{\Omega}_b \times \mathbf{r}^{CG,k} + \Omega_b \times (\Omega_b \times \mathbf{r}^{CG,k}) + \sum_i \Phi_{\eta_i}^{*,k} \ddot{\eta}_i \quad (19)$$

with $\Phi^{*,k}$ being a submatrix of the modal matrix Φ considering only the node related to the measurement position k in the three translational directions for the considered modes i . Note that the latter entries of the

matrix are unknown and subject to the parameter estimation. The stress at a given measurement location on the flexible structure is a linear combination of the individual contributions of each normal mode. For a linear stress-strain relationship, the strain behaves in the same manner at location k ,

$$\epsilon^k = \epsilon_0^k + \sum_i \epsilon_i^k \eta_i + \epsilon_T^k (T - T_{ref}) \quad (20)$$

where ϵ_0^k corresponds to the zero term or bias in the strain measurement, ϵ_i^k is the effect of the i th normal modal deflection on the strain output, and ϵ_T^k is used to compensate the effects of air temperature changes with T_{ref} as an arbitrary temperature level of reference.

Using these accelerometer and strain gauge measurements in addition to inertial and atmospheric measurements, a system identification in the time domain is performed in order to identify the model structure and estimate the parameters of the flexible glider simulation model. Step by step, five different structural modes (four wing bending and one lateral fuselage bending) were included in the model after identification of the rigid-body dynamics [62–64]. As an example, Fig. 12 provides time history comparison plots of measurements and simulation outputs after identification for the sole rigid-body and the full flexible glider model. It is clearly visible that the inclusion of the structural dynamics significantly enhances the model's ability to represent the measurements. Hence, these results show the possibility

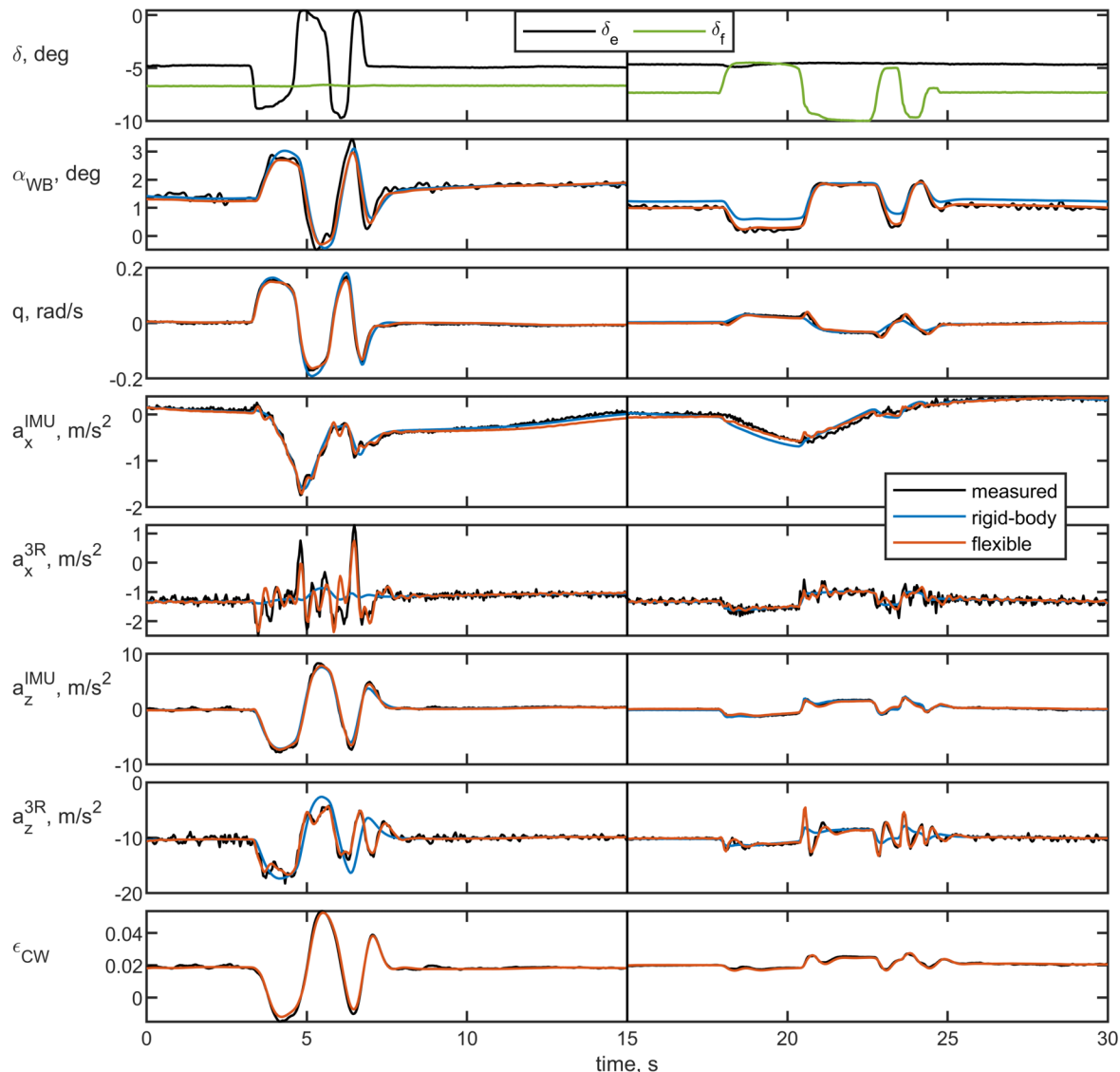


Fig. 12 Time history plots of rigid-body and flexible models for longitudinal 3211 maneuvers (elevator and flap deflection) at 160 km/h; refer to Fig. 11 for meaning of symbols.

of a combined rigid-body and structural dynamics model identification in time domain (including mode shapes) with suitable measurements from flight tests. The identification of such a hybrid-flexible model for a large transport aircraft using frequency-domain identification is described in chapter 16 of Ref. [2]. Similarly, this hybrid-flexible modeling approach has been successfully applied to the ACT/FHS helicopter as shown in Sec. V.C.

D. Loads Monitoring

In 2014, DLR started the development of a rigid-body multipoint loads model based on flight-test data using time-domain system identification techniques. For this work, a Discus-2c sailplane served as a flight-test platform: a single-seat high-performance sailplane manufactured by Schempp-Hirth Flugzeugbau GmbH (Fig. 13). It was equipped with a special flight-test instrumentation composed of inertial and GPS sensors, control surface deflection sensors, a five-hole probe nose boom, 46 strain gauge sensors, 20 fiber Bragg gratings, and 15 three-axis accelerometers at different aircraft locations.

There were no sensors to measure the loads directly. The loads have to be calculated from the strain gauge and/or the fiber Bragg grating measurements; in other words, these sensors have to be calibrated. To generate a database for these calibrations, extensive ground tests in a hangar were performed [65]. By placing sand bags of known weight on various places on the aircraft's structure, more than 500 static load cases were generated. For seven load stations, six on the wing and one on the tail, the true loads were calculated from the known weights and positions of the sand bags. The parameters of the calibration equations were estimated to enable the calculation of the structural loads (shear force V , bending moment M , and torque T) at the seven load stations from the strain gauge and fiber Bragg grating measurements. In Ref. [65], various practical pitfalls of the calibration process and the issue of selecting the best combination of sensors for the calculation of the local structural loads are discussed. As an example of the final quality of the calibration, Fig. 14 gives the proof of match between the calibration equation output for the shear



Fig. 13 DLR Discus-2c Sailplane as flight-test platform for loads data generation.

force at the right wing load station WR1 (0.82 m from the symmetry plane of the aircraft) and the real applied loads for almost 300 calibration load cases.

Having the calibration equations available, the next step was to formulate different models allowing a load calculation in simulation, in other words, not from measurements but from physics-based models accounting for inertial and aerodynamic forces and moments. As an extension of the two-point model formulation separating wing and horizontal tail influences on aerodynamics [66], a three-point model (left and right wing, horizontal tail) was developed and identified [67,68]. Additionally, a so-called seven-point model that allows the computation of local loads (shear, bending, and torsion) at seven load stations (three on the left wing, three on the right wing, and one at the horizontal tail) was introduced and identified.

In a subsequent step, the Discus-2c glider was equipped with Micro-Electro-Mechanical-System (MEMS) pressure sensors to measure the aerodynamic loads present on the airplane's wing during flight. Having the calibrated results from the strain measurements, the quality of the loads derived from the MEMS pressure sensor measurements could be assessed during the flight test [69,70].

V. Rotorcraft Models

The vast majority of rotorcraft system identification performed at DLR pertains to the ACT/FHS where models of different complexity are needed for simulation and flight control law development. As models are required for the whole flight envelope, dedicated flight tests with frequency sweep and multistep inputs (3211 or 2311) in all controls were performed at five reference speeds (hover and 30, 60, 90, and 120 kt) and yield the database for all system identification efforts.

A. Rotor

According to Ref. [2], models of the ACT/FHS to be used for flight control development should accurately cover the frequency range of 1–15 rad/s. But experience has shown that this frequency range is too narrow and has to be extended at the lower end for flying with external loads and at the upper end to avoid exciting structural modes. The aim was thus to develop models that are accurate over the frequency range of 0.5–30 rad/s. This means that an extended model structure that explicitly includes the regressive flapping, coupled inflow/coning, and regressive lead/lag states of the rotor is necessary.

1. Flapping

In state-space identification with a six-degree-of-freedom (DOF) model, the fuselage motion is described by a fully coupled quasi-steady model structure. The rotor is treated as an actuator disk, comparable to control surfaces on a fixed-wing aircraft. The time

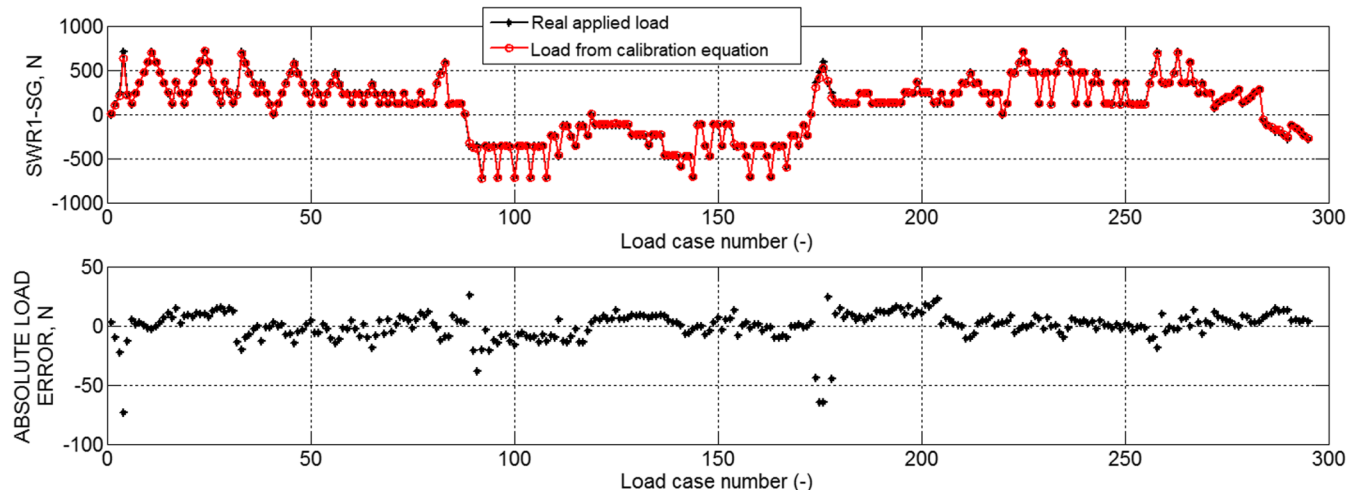


Fig. 14 Comparison of real and calibrated shear forces measured by a strain gauge sensor at the right wing load station WR1 and the error between them, from Ref. [67].

of the transient rotor response is taken into account by equivalent time delays on the cyclic controls.

Even though the on-axis responses in pitch and roll can be adequately described by a 6-DOF model, Fig. 15 shows that the match in the cross-axis responses to cyclic control inputs (roll rate due to longitudinal cyclic p/δ_{lon} and pitch rate due to lateral cyclic q/δ_{lat}) is not satisfactory. Neither the amplitude nor the phase is modeled correctly. To improve this match, an additional specific rotor dynamic phenomenon, the regressive flap response, has to be accounted for.

Rotor flapping is usually accounted for in system identification modeling with the explicit formulation developed by Tischler et al. (chapter 15 in Ref. [2]). This explicit formulation includes two coupled first-order differential equations for the longitudinal and lateral flapping angles that are triggered by the longitudinal and lateral cyclic control inputs. Alternatively, an implicit formulation of the flapping equations as first described in Ref. [71] can be used where the flapping angle equations are inserted into the equations for pitch and roll rate, resulting in pitch and roll acceleration as two additional state variables.

In Ref. [72], it is shown that the explicit and the implicit formulations of the rotor flapping dynamics produce equivalent results. The tradeoff between implicit and explicit modeling of the flapping dynamics in the context of rotor state feedback is discussed in Ref. [73].

Figure 15 shows that an 8-DOF model that accounts for the flapping dynamics provides a much better match of the phase at higher frequencies for the cross-axis responses. For pitch due to lateral input, the amplitude at higher frequencies is also improved. The model improvement by accounting for flapping in case of the Bell 412 helicopter is demonstrated in Refs. [74,75].

2. Inflow/Coning

The vertical response to collective input at low frequencies (below 1 rad/s) is dominated by the first-order helicopter heave damping characteristic. At mid to high frequencies (about 1–12 rad/s), the vertical response is characterized by the coupled inflow/coning dynamics. The inflow describes the air-mass dynamics of the lifting rotor that cause transient rotor thrust effects, and coning is the symmetric deflection of the rotor blades. At higher frequencies, the response is dominated by the second-order coning dynamics with a natural frequency of about once per revolution. The exact frequency depends on hinge offset and flapping stiffness.

Figure 16 compares the resulting frequency response of vertical acceleration due to collective control input a_z/δ_{col} for different modeling approaches using numerical values of the ACT/FHS. The first curve is based on the quasi-static model $\dot{w} = Z_w w + Z_{\delta_{\text{col}}} \delta_{\text{col}}$. It

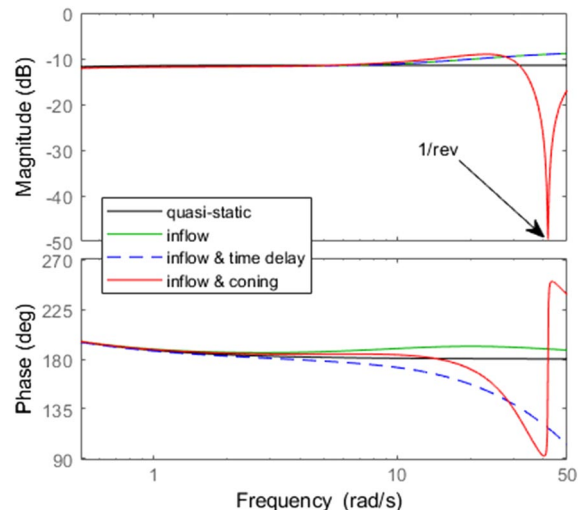


Fig. 16 Simulated frequency responses for a_z/δ_{col} using different models (ACT/FHS in hover), adapted from Ref. [76].

can be seen that the quasi-static formulation leads to flat amplitude and phase curves at higher frequencies.

An implicit model that includes the first-order inflow equation and accounts for coning through an equivalent time delay is derived in Ref. [71]. The second curve in Fig. 16 is a simulation of the corresponding transfer function. It shows that accounting only for inflow and not for coning leads to a rising amplitude in the vertical response at higher frequencies but yields no phase reduction. The third curve in the figure illustrates that the phase drop that is caused by the coning can approximately be accounted for if the implicit model is extended by an equivalent time delay.

The approach most widely used for modeling the inflow/coning dynamics and their coupling to the fuselage is the hybrid formulation developed by Tischler et al. (chapter 15 in Ref. [2]). The fourth curve in Fig. 16 is the corresponding vertical acceleration response. It can be seen that the hybrid model with inflow and coning leads to a transfer function zero and thus a large drop in amplitude at the rotor frequency.

All these different modeling formulations are applied to ACT/FHS flight-test data and compared in Ref. [76]. The hybrid model provided a good match for frequencies up to 15 rad/s, which is sufficient for many flight dynamics and control applications. However, the goal was to extend the model validity up to 30 rad/s. Because of its bearingless design, the rotor of the ACT/FHS has a relatively large

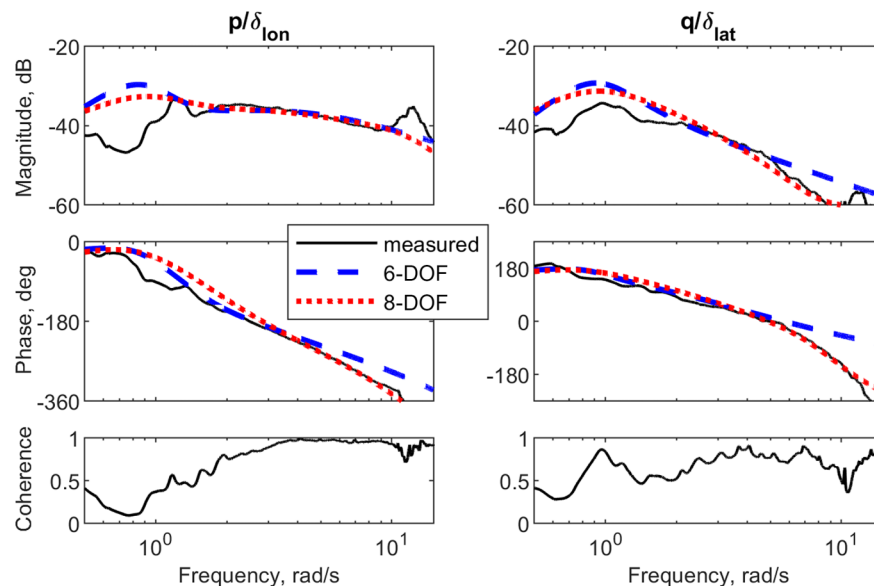


Fig. 15 Improvement of the cross-axis responses of a 6-DOF ACT/FHS model in hover by accounting for flapping (8 DOF).

equivalent hinge offset of 10%, but the hybrid formulation was developed assuming small hinge offsets. Thus, the coning equation of the hybrid model had to be extended to include the influence of hinge offset. Furthermore, two parameters of the hybrid model had to be estimated instead of using the theoretical predictions to finally arrive at the match shown in Fig. 17. Details of these model extensions can be found in Ref. [76].

3. Regressive Lead/Lag

Unlike for regressive flap responses to cyclic inputs, no simple physical modeling exists for the coupled state-space equations for the lead/lag motion. Therefore, a modal approach is usually taken, where two closely spaced complex pole/zero pairs (dipoles) with a common denominator are appended to the pitch and roll rate responses to account for the effect of the regressive lead/lag; see chapter 15 in Ref. [2].

For the ACT/FHS, a slightly different approach is used where the dipoles transform the cyclic control inputs δ_{lon} , δ_{lat} ; in other words, the dipoles are added on the input side and not on the outputs of pitch

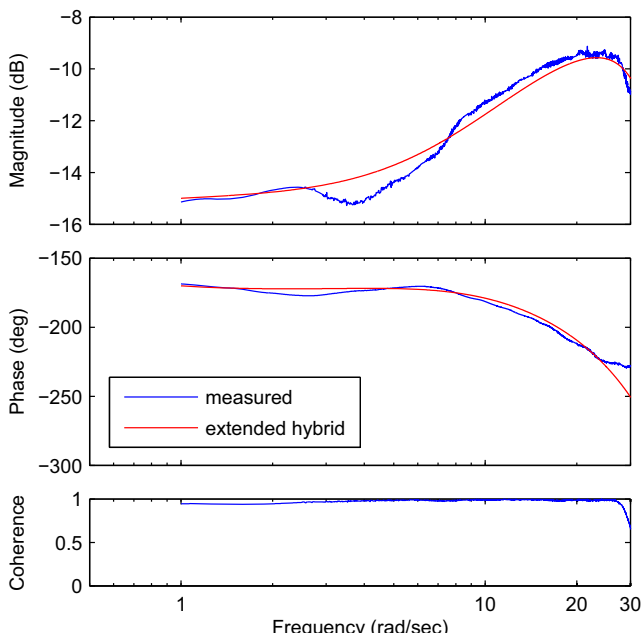


Fig. 17 Match in a_z/δ_{col} of the identified extended hybrid model in hover, from Ref. [76].

and roll rate p , r . The reason for this is the fact that the effect of the regressive lead/lag for the ACT/FHS is not only present in the on-axis responses (p/δ_{lat} and q/δ_{lon}) but is also very pronounced in the cross-axis responses (p/δ_{lon} and q/δ_{lat}).

Whereas the lead/lag effect in the on-axis responses is modeled equally well with both approaches, the left part of Fig. 18 shows that the lead/lag effect in the cross-axis response of the ACT/FHS is better captured by the model with two dipoles at the inputs and not by the usual formulation with dipoles at the outputs. Another advantage of the model formulation with the dipoles at the inputs is that influences of the lead/lag on the longitudinal and lateral accelerations that are present in ACT/FHS data can be captured as can be seen in the right part of the figure. A thorough discussion of the different variants of lead/lag modeling that also includes another formulation with only one complex dipole is found in Ref. [77].

B. Engine

After accounting for the rotor degrees of freedom of flapping, inflow, and regressive lead/lag, the identified models of the ACT/FHS still had deficits in the response of the yaw rate due to collective input that were attributed to unmodeled engine dynamics.

Accounting for engine dynamics by a simple lag in the influence of collective input on the angular rates was not sufficient. A regression analysis of the yaw rate using measured data for rotor speed Ω and engine torque Q showed that torque has a profound influence on the yawing motion, whereas no direct influence of rotor speed could be found. Thus, torque modeling with a dynamic engine model was needed.

First, the frequency responses for rotor speed due to collective and pedal inputs were approximated by transfer functions. For inclusion in the identification model, these frequency response models were converted into a state-space model and combined with a Taylor series model for the torque dynamics. The parameters of this engine model were identified for each of the five reference speeds with the ML frequency-domain method using collective and pedal sweep maneuvers. The resulting engine model was simplified by fixing those model parts that were constant over the whole flight envelope. More details about this approach can be found in Ref. [77].

Finally, the identified engine model was coupled to the overall model. Figure 19 shows the match in the frequency responses of yaw rate due to pedal and collective inputs (r/δ_{ped} and r/δ_{col}) in hover for the models with and without engine modeling. As expected, the yaw rate response to collective input improves both in amplitude and in phase. Interestingly enough, the yaw response to pedal inputs (on-axis response) improves also.

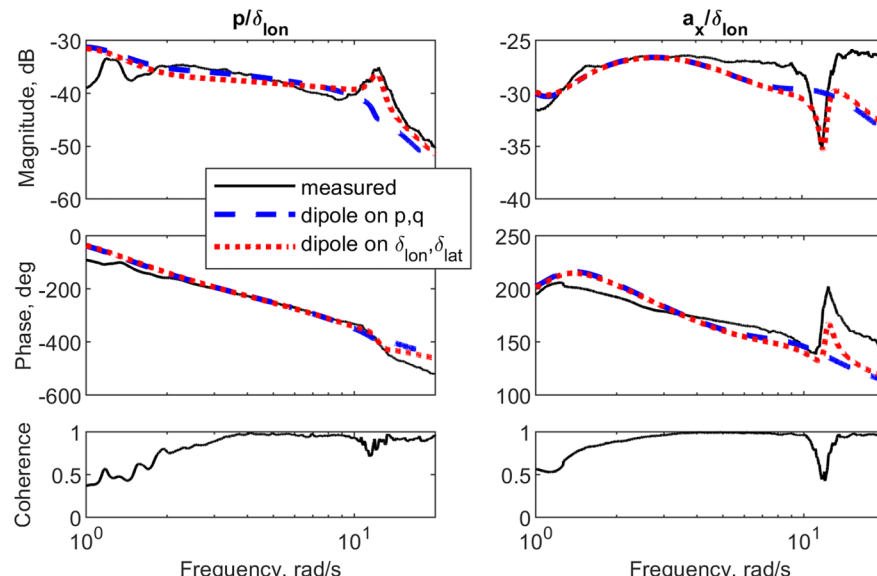


Fig. 18 Match in roll rate and longitudinal acceleration due to longitudinal cyclic input for both lead/lag models (hover), adapted from Ref. [77].

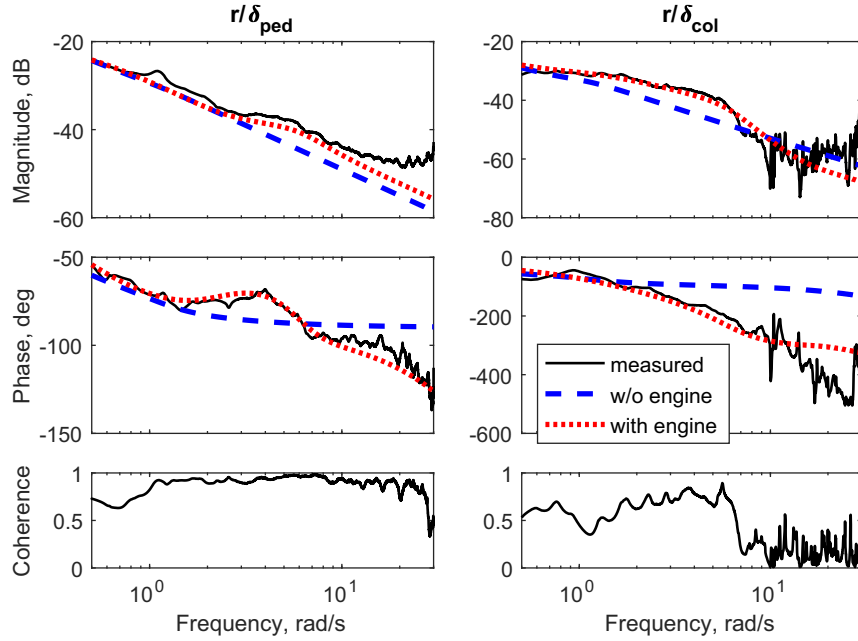


Fig. 19 Improvement of yaw responses by engine modeling (ACT/FHS in hover), from Ref. [77].

A more detailed physics-based engine model would require measured engine parameters (at least fuel flow) which are not available in the ACT/FHS test data. Therefore, in Ref. [21], an improved engine model was identified using the PBSIDopt method (Sec. II.A.3) and then coupled to the physics-based helicopter model. The inputs for this engine model were the four pilot controls (δ_{lon} , δ_{lat} , δ_{col} , and δ_{ped}) as well as the vertical velocity w and yaw rate r to account for coupling effects. The outputs were rotor speed and torque, and a model order of $n = 4$ was selected.

Figure 20 shows the match for the PBSIDopt model in comparison to the ML-derived model described previously. It can be seen that both models perform comparably well for collective inputs (third column from the left) but that the PBSIDopt model performs better for all other control inputs. This would be expected because the ML-derived model does not account for the influence of the cyclic control inputs on rotor speed and torque and contains no coupling to w and r .

More details on the derivation of this improved engine model and its coupling to the helicopter model are found in Ref. [21].

C. Structural Modes

To ensure satisfactory handling and ride qualities, increasingly higher crossover frequencies are required in the flight control systems. Flight control law design is usually conducted using linear models that describe the rigid-body dynamics and, if required, also rotor and/or engine dynamics. As long as the structural modes remain well separated from the crossover frequency (by a factor of at least 10–15 [78]), notch filters are sufficient to avoid potential interaction with the structural modes. Otherwise, the flexible modes have to be accounted for in the models used for control system design.

At the time when the notch filters were designed for the ACT/FHS, excitation of the tail vertical mode had not yet been experienced for collective inputs. The corresponding frequency was therefore only

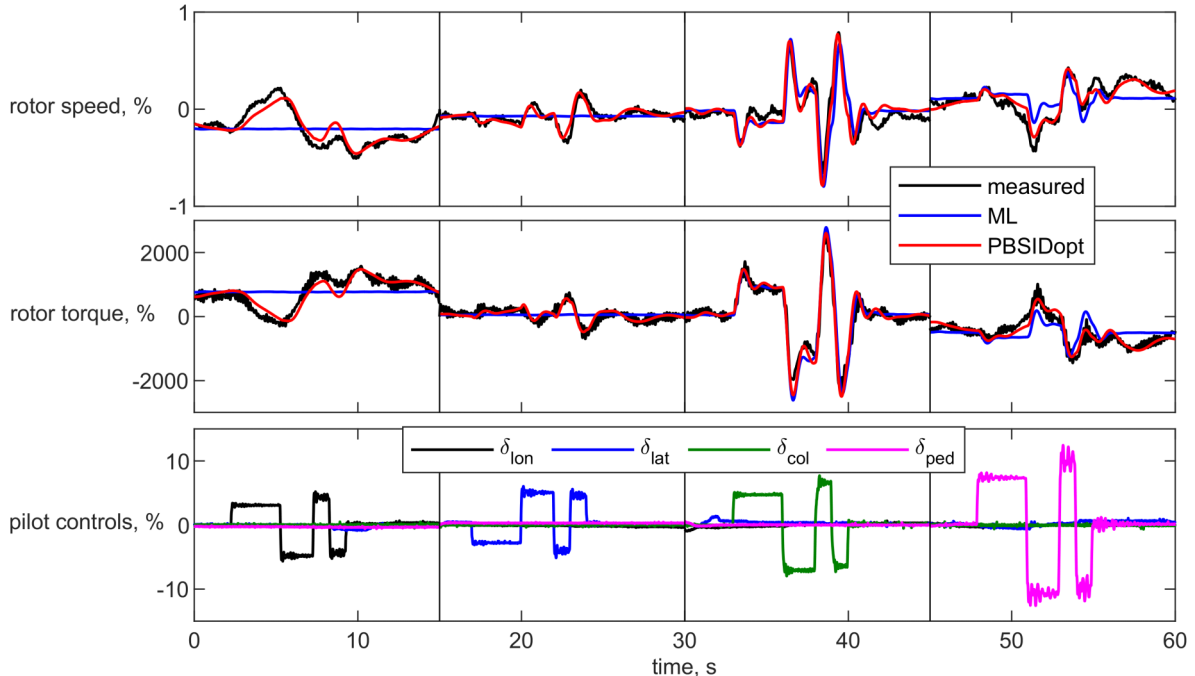


Fig. 20 Time-domain comparison of physics-based (ML) and blackbox (PBSIDopt) engine model, adapted from Ref. [21].

accounted for in the notch filters for the cyclic and not the collective control input. This resulted in excitation of the tail vertical mode in system identification tests with computer-generated multistep inputs.

Unlike the sailplane used for structural load modeling in Sec. IV.D, the ACT/FHS is not equipped with dedicated sensors to measure structural deformations except for strain gauges at the tail. As matching the strain gauge signals was not deemed necessary, the same instrumentation as used in the rigid-body/rotor/engine modeling efforts was also used for the derivation of models including flexible modes.

As the influence of tail flexibility for the ACT/FHS is most pronounced in pitch rate q due to collective control input δ_{col} , the corresponding transfer function was first investigated as a single-input/single-output (SISO) system. A first-order response was assumed for the rigid-body part of q/δ_{col} . Following the approach from chapter 16.4 of Ref. [2], one second-order system for the tail vertical mode was then added in a partial fraction expansion

$$\frac{q}{\delta_{\text{col}}} = \frac{M_{\delta_{\text{col}}}}{s - M_q} + \frac{S_{\delta_{\text{col}}}s}{s^2 + 2\zeta_{\text{str}}\omega_{\text{str}}s + \omega_{\text{str}}^2} \quad (21)$$

where ω_{str} , ζ_{str} denote the frequency and damping of the structural mode and $S_{\delta_{\text{col}}}$ is the control derivative.

For identification, this partial fraction model was augmented by a time delay to account for unmodeled rotor dynamics. Identification was performed using the frequency response method and a frequency range of 10–40 rad/s. Figure 21 illustrates the match of the identified SISO model in the time domain for a 3211 maneuver. The oscillation in pitch acceleration \dot{q} is modeled correctly, and the remaining error is very small. As only a SISO model for pitch due to collective was used, the match in the pitch rate is of course not as good as for a fully coupled model.

It is important to note that the identification of this simple extended model is based solely on the fuselage angular response sensors and does not require additional flight-test measurements of the structural response.

Assuming that the elastic displacements are small compared to the rigid-body motion, the dynamics of the flexible modes can be written with respect to a body-fixed mean axis system, a formulation commonly used in flight dynamics and control literature [78]. This means

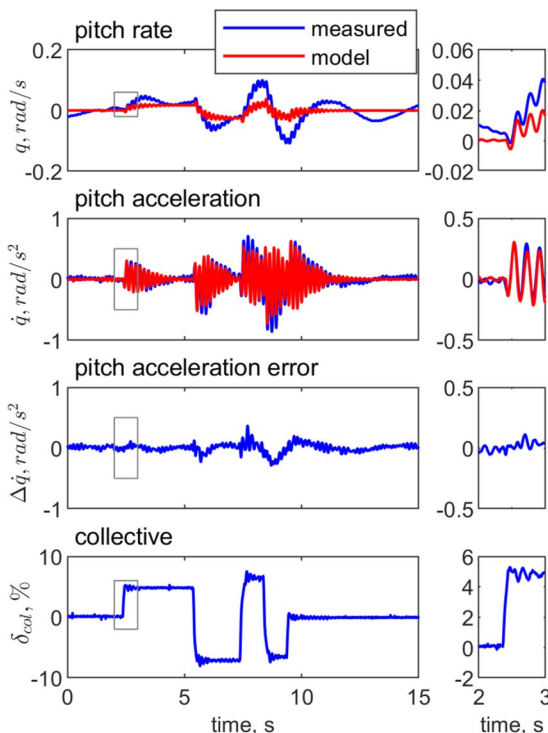


Fig. 21 Time-domain match of the SISO model for q/δ_{col} with added structural mode, from Ref. [79].

that the matrices of the coupled rigid-body/structural modes state equations can be partitioned as [2]

$$\mathbf{A} = \begin{bmatrix} \text{rigid-body stability derivatives} & \text{aeroelastic coupling terms} \\ \text{rigid-body coupling terms} & \text{structural flexibility modes} \end{bmatrix} \quad (22)$$

and

$$\mathbf{B} = \begin{bmatrix} \text{rigid-body control derivatives} \\ \text{structural mode control derivatives} \end{bmatrix} \quad (23)$$

and the state vector is also partitioned into rigid-body and structural components as

$$\mathbf{x} = \begin{bmatrix} \mathbf{x}_{\text{rb}} \\ \mathbf{x}_{\text{str}} \end{bmatrix} \quad (24)$$

The rigid-body states \mathbf{x}_{rb} correspond to the motion of the fuselage reference axes. The structural state vector \mathbf{x}_{str} consists of the generalized displacement and rate (velocity) state for each structural mode to be considered. The number of structural modes to be included depends on the frequency range of interest.

A fully coupled model as in Eq. (22) can only be identified when additional sensors like strain gauges and accelerometers at different positions throughout the flexible vehicle are available as was the case for the flexible sailplane described in Sec. IV.D. Without such extra instrumentation, simplifications have to be made to arrive at a model structure where all model parameters are uncorrelated and identifiable.

Dropping both the rigid-body and the aeroelastic coupling terms in Eq. (22) leads to state equations where the rigid-body and structural modes are dynamically decoupled. The influence of the modal states on the output variables in such a dynamically decoupled system is solely described by influence coefficients in the measurement equations.

In the ACT/FHS case, the state equations of the 17th-order model that accounts for rigid-body dynamics, rotor flapping, inflow, regressive lead/lag, and engine dynamics were extended by one modal state for the tail flexibility. For the identification of the flexible mode, the parameters of the 17th-order model were kept fixed, and only the parameters of the structural modes were estimated. The identification was performed with the ML method in the frequency domain, and a frequency range of 10–40 rad/s was used, as the frequency range of 0.5–10 rad/s is already well covered by the 17th-order model whose parameters remain unchanged.

Figure 22 shows the resulting match in the transfer functions from collective control input to pitch rate and longitudinal and lateral acceleration in comparison to the 17th-order model without added flexible mode. It can be seen that by including the influence of tail flexibility the match in amplitude and phase for q/δ_{col} is clearly improved in the high-frequency range. Unlike for the SISO model, the influence of tail flexibility is now also modeled in the transfer functions a_x/δ_{col} and a_z/δ_{col} .

As mentioned before, the generalized multiple-input/multiple-output (MIMO) flight dynamics model from Eq. (22) includes full two-way dynamic coupling between the rigid-body and the elastic states. This yields a complex identification model structure with many associated identification parameters and considerable parameter correlation and is thus not well suited to identification from flight-test data. In many applications, although the coupling of the rigid-body dynamics into the elastic states (rigid-body coupling) must be included for satisfactory modeling accuracy, the dynamic coupling of the elastic states into the rigid-body equations of motion (aeroelastic coupling) can be assumed to be quasi-steady. If only the most significant terms in the dynamic coupling of the rigid-body dynamics into the elastic states are retained, this leads to a so-called hybrid model structure, which is a one-way coupled formulation (chapter 16.4 of Ref. [2]).

When the one-way coupled equations for the hybrid model of the ACT/FHS were built, it was assumed that only the longitudinal states

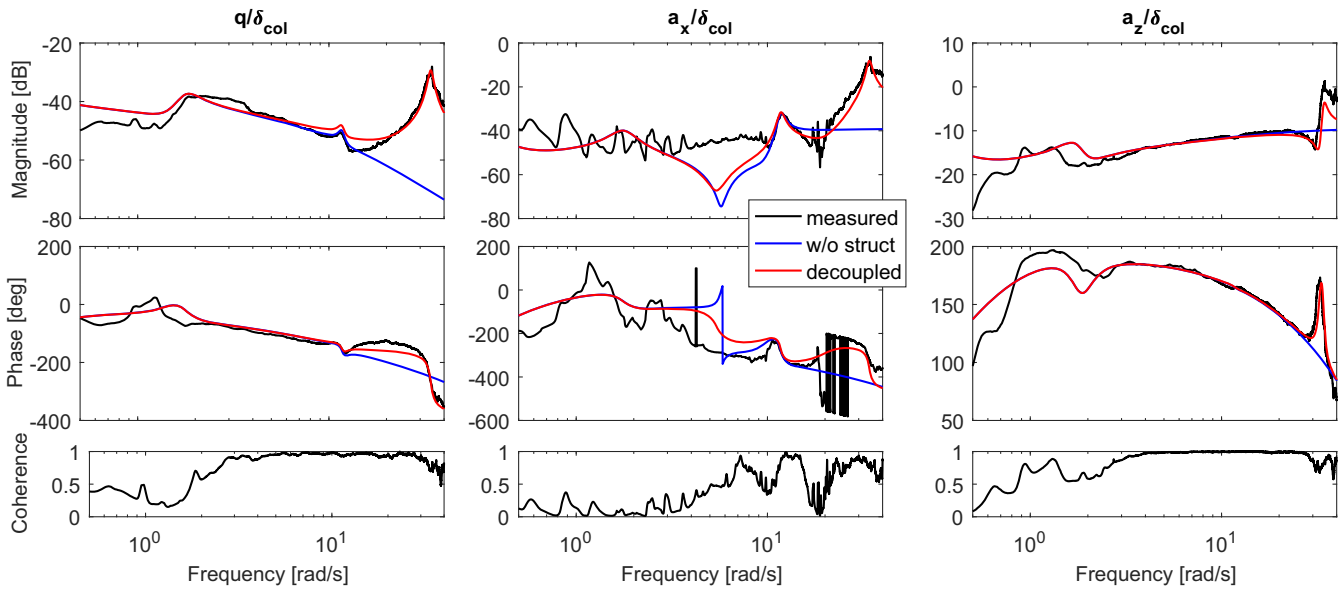


Fig. 22 Frequency-domain match of the MIMO model with decoupled structural mode (ACT/FHS at 60 kt), from Ref. [79].

u , w , and q have an influence on the vertical tail elastic mode. Identification was again performed with the ML method in the frequency domain.

Figure 23 compares the match of the 17th-order model without flexible modes, the decoupled model, and the hybrid model. It can be seen that by introducing the one-way coupling between the rigid-body and the modal states the match in q/δ_{col} is improved even further. In addition, the influence of the structural mode is now extended to the cyclic control inputs δ_{lon} and δ_{lat} .

A more thorough discussion of the identification of structural modes for the ACT/FHS can be found in Ref. [79].

D. Non-Physics-Based Models

Defining an appropriate model structure and setting the corresponding initial values to identify physical rotorcraft models can be complicated and time consuming. Even if missing dynamics can be related to physical effects, enhancing an existing model structure accordingly is not an easy task. If the existing models are complex, like the ACT/FHS models, this task becomes more and more complicated, as connections between different submodels have to be accounted for and their parameters have to be chosen carefully, which

was illustrated in the previous sections. The PBSIDopt method does not require a predefined model structure nor initial values but only requires three integer parameters to work: model order n , past window length p , and future window length f . The resulting linear discrete-time state-space models usually have nonphysical states, and due to the included model reduction step, the model's eigenvalues often do not have a corresponding physical mode. In this sense, the PBSIDopt method yields blackbox models.

In this section, system identification results using the PBSIDopt method using 60 kt ACT/FHS data are shown. The four helicopter controls for longitudinal and lateral cyclic, pedal, and collective are used as system identification inputs. The body-fixed airspeed components u , v , w ; the angular rates p , q , r ; and the roll and pitch attitude angles Φ and Θ of the rotorcraft are used as outputs to be matched.

In addition to the model order n , the past window length p and the future window length f affect the identified models, and choosing an optimal p and f is still active research. For this reason, a parameter variation study with respect to p , f , and n was conducted where a huge range of suitable parameter settings was tested and evaluated. Model orders n between 8 and 20 were investigated. The past window

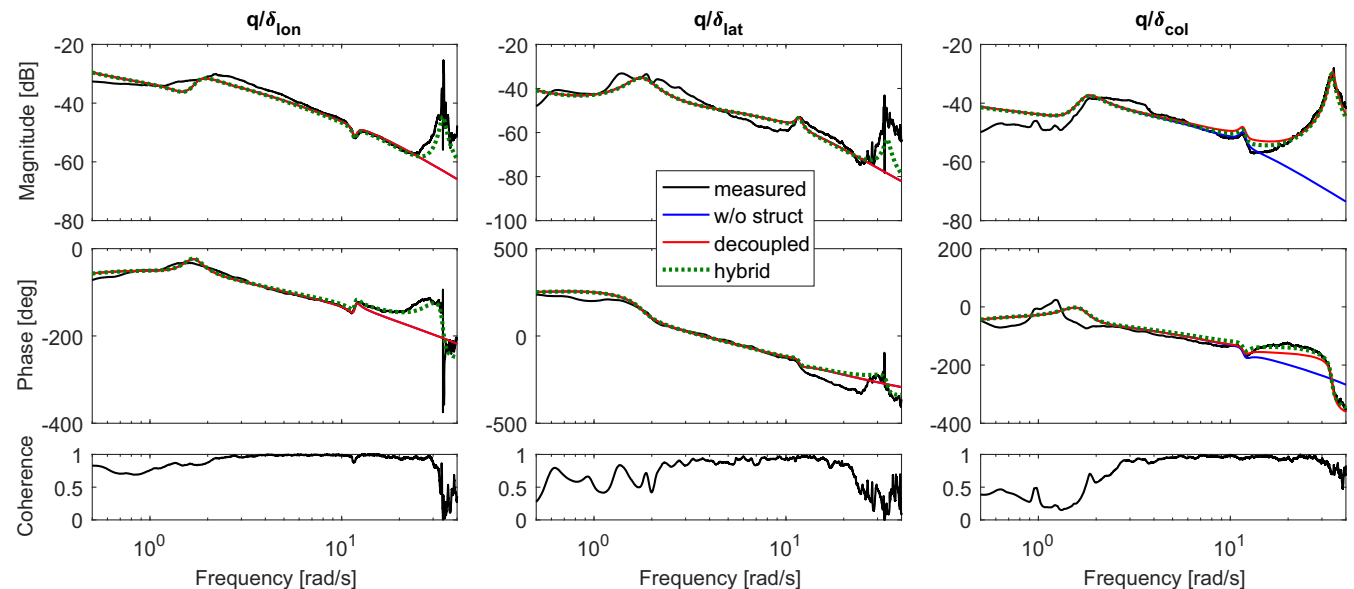


Fig. 23 Frequency-domain match of the hybrid MIMO model (ACT/FHS at 60 kt), adapted from Ref. [79].

length p was varied between n and 994 (the maximum number possible for the used flight-test data), and the future window length f was varied between n and p . In summary, between 5050 (for $n = 20$) and 6261 (for $n = 8$) models were identified for each model order. The overall identification and validation process took about 48 h on a standard desktop computer.

An appropriate model order can be chosen based on the method's cost function. In this case, a model order of $n = 18$ was selected, because these models include most of the dynamics in the frequency range of interest and have about the same order as the most advanced physics-based models of the ACT/FHS.

In Fig. 24a, the distribution of all identified model's transfer functions from lateral cyclic input δ_{lat} to roll rate p are shown. All transfer functions are located between the dotted black lines showing the maximum and minimum magnitude/phase. The mean magnitude/phase is shown in solid black, and the standard deviation (std) around the mean is depicted in shaded gray. The FR generated from the flight-test sweeps are plotted in blue, the transfer function of the 17th-order physical model (phy-n17) is plotted in red, and the best PBSIDopt model is plotted in yellow.

Huge variations in magnitude and phase can be seen in Fig. 24a at low frequencies. It is obvious that the choice of p and f significantly changes the resulting model. Various models exhibit weakly damped resonances, some of them unstable, in the midfrequency range from 4

to 9 rad/s. The variations between the identified models increase for low and high frequencies.

In Fig. 24b, 50 models with the lowest cost function are selected (50 best PBSIDopt models). The transfer function shown in yellow is the same as in Fig. 24a. The distribution of these 50 models is very tight and matches the measured frequency response very well for the mid-frequency range. Nonetheless, some deficiencies can be found. At first, every selected model of these 50 best shows a distinct resonance at about 0.3 rad/s. This resonance can be assigned to the phugoid of the ACT/FHS, but here the damping is too low. Additionally, the regressive lead/lag at about 12 rad/s is overdamped, and, finally, these models do not match the measured FR for frequencies above the regressive lead/lag. These model deficiencies are induced by the underlying ARX model with very high p and the resulting high variance of the ARX model. Consequently, choosing an appropriate PBSIDopt model solely by the lowest cost function can result in limited model fidelity.

In Ref. [15], a criterion for selecting *candidate models* from all identified models based on the stability of the predictor form system matrix A_K is presented. Only models with a spectral norm below a user-defined threshold are accepted, and the best models are then selected from the remaining valid ones. Here, the 50 candidate models are different from the 50 best models shown in Fig. 24b.

The distribution of 50 candidate models that were selected using this criterion is shown in Fig. 25 for lateral cyclic to roll rate on the left and

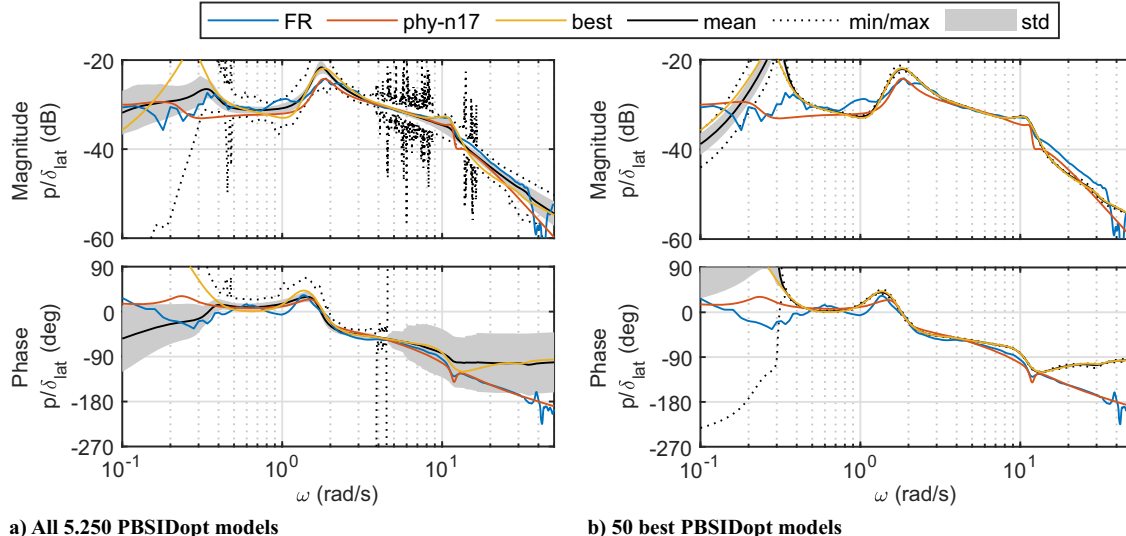


Fig. 24 Distribution of identified PBSIDopt transfer functions from lateral cyclic δ_{lat} to roll rate p and measured frequency responses, $n = 18$.

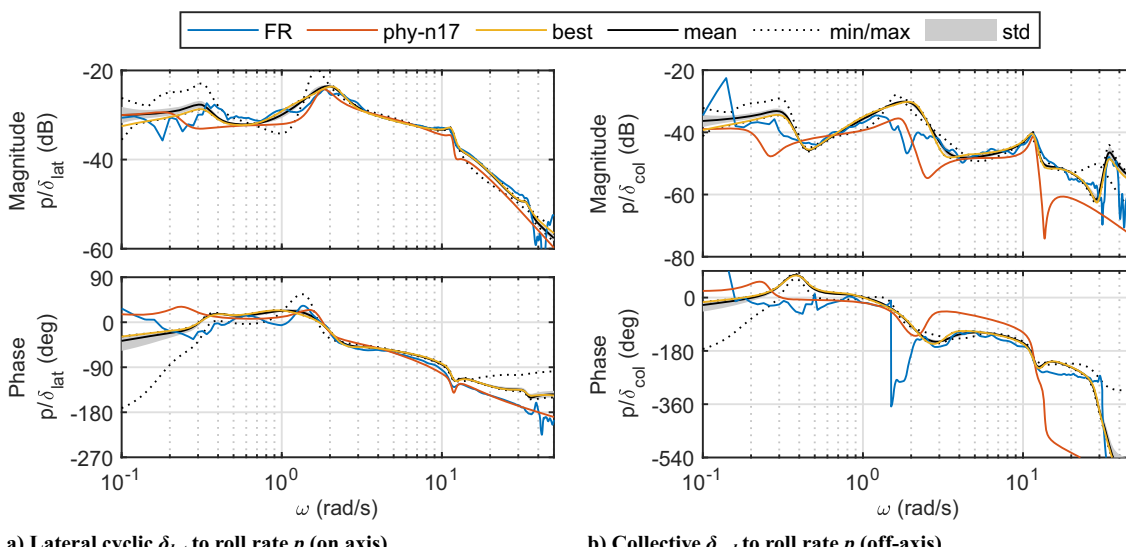


Fig. 25 Distribution of the transfer functions of 50 selected PBSIDopt candidate models with $n = 18$ and measured frequency responses.

collective to roll rate on the right. Comparing Fig. 25a with Fig. 24b, the mentioned deficiencies vanish for the chosen candidate models. These models match the measured FR very well for the whole frequency range of interest. The off-axis performance of the candidate models can be investigated in Fig. 25b. The models' magnitude and phase reproduce the FR accurately. The PBSIDopt models also include the structural mode at about 35 rad/s, as mentioned in Sec. V.C, which is not included in the 17th-order physical model. The fluctuations of the measured FR around 1.5 rad/s are caused by very low coherence (not shown in Fig. 25b) and are consequently not covered by the models.

The PBSIDopt method has been successfully applied to ACT/FHS data and has shown very good model performance and applicability [15,16,39,80,81]. Furthermore, it was compared to other rotorcraft system identification tools and methods using data from flight tests with the Bell 412 ASRA of the National Research Council (NRC) Canada in Ref. [74].

E. Rotor Mast Moment Observer

Incorporating main rotor states like the tip-path-plane flapping angles or rotor mast moments into the rotorcraft flight control laws allows for enhanced handling and ride qualities as well as reduced pilot workload. As measuring the rotor states in the rotating frame is cost intensive and associated with a high technical effort, using estimation algorithms (i.e., observers) instead of data from sensors in the rotor system was investigated.

The main rotor measurement system of the ACT/FHS depicted in Fig. 26 provides rotor azimuth and main rotor mast bending moments. Data transmission between the rotating and nonrotating frame is handled by telemetry using high-frequency antennas. Rotor



Fig. 26 Sensor signal processor system of ACT/FHS's rotor measurement system.

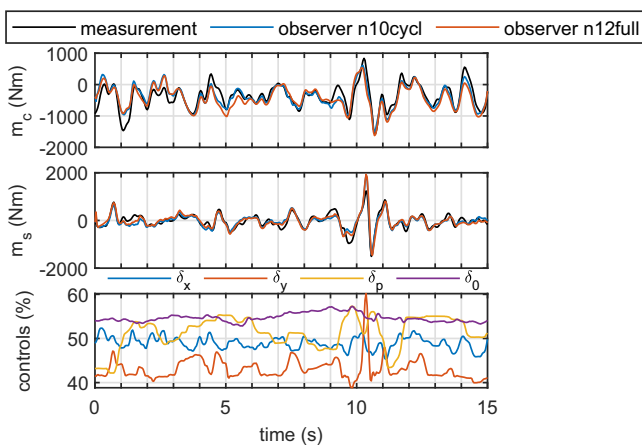
blade flapping signals are currently not measured, as the blades have not been instrumented yet. Therefore, data-driven observers to replicate the measured rotor mast moments in the rotorcraft-fixed frame using only rigid-body measurements were designed.

Several linear models were identified that describe the response of the rotor mast moments in pitch m_c and roll m_s . A physics-based model for the mast moments was identified with the ML method, and blackbox models of different complexity were identified with the PBSIDopt method. Some of the blackbox models used all four pilot controls as input variables, whereas reduced models using only the two cyclic controls were also identified. More details can be found in Ref. [81].

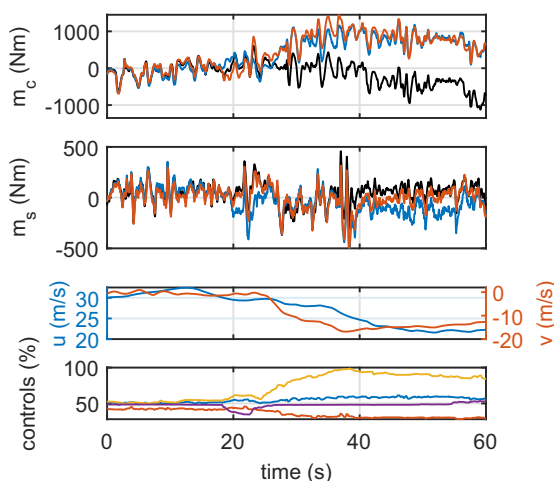
The most promising models were then used to design rotor mast moment observers. The observer design process was separated into three steps. First, the observer was designed as a steady-state Kalman filter, which guarantees stable observer dynamics. Next, the observer gain was tuned using flight-test data. Two different observer design configurations are evaluated in Ref. [81]. Finally, a cross-validation procedure was conducted on a carefully compiled data set covering the most commonly encountered flight conditions to select the optimal observer configuration.

The time-domain results of two selected optimal observers are compared. The first observer *n10cycl* is designed using a tenth-order model for the main cyclic axis of the rotorcraft and incorporates the two cyclic controls as well as roll and pitch rate. The second observer *n12full* is based on a full 12th-order model and includes all four control inputs as well as roll, pitch and yaw rate, and vertical speed. Figure 27a shows the measured and estimated rotor mast moments from both observers for a section of forward flight in moderate turbulence (rated as level 6 based on Ref. [82]). In general, the performance of both observers is very good despite the turbulent excitation of the rotorcraft. The estimated rotor mast moments do not suffer from noteworthy time delays, and the short-term behavior seems adequate. In detail, both observers exhibit comparable lateral mast moment m_s estimates, while the less complex *n10cycl* observer performs slightly better for the longitudinal axis m_c after $t = 4$ s.

The measured and estimated mast moments during a coordinated turn are compared in Fig. 27b. The measured rotor mast moments are accurately reproduced during the first 20 s of the run. Then, the estimated longitudinal mast moments m_c slowly diverge from the measurements as the rotorcraft starts to turn. During the turn, headwind becomes crosswind, which is then compensated by roll angle and lateral cyclic as well as pedal inputs. In an analogous manner, forward (air)speed is reduced, and longitudinal cyclic input and pitch angle are adjusted. Hence, this maneuver violates the near-trim validity of the underlying models and therefore cannot be covered by the observer unless changing trim conditions are accounted for in



a) Flight in moderate turbulence



b) Coordinated turn with head- and crosswind

Fig. 27 Time-domain comparison of measured and estimated rotor mast moments, from Ref. [81].

its design. Still, the mid- and high-frequency components of the estimated rotor mast moments match the measurements.

More details about the model identification, the observer design, and the evaluation of the observers can be found in Ref. [81].

F. Model Stitching

Identified linear state-space models represent the dynamic response of an aircraft for a discrete reference flight condition and configuration and are accurate within some limited range around the reference condition. These discrete point linear models are suitable for point control system design and point handling qualities analyses. However, a single, wide-envelope model is desirable for full-mission simulation. Model stitching combines so-called linear anchor point models and trim data for discrete flight conditions with nonlinear elements to produce a single, nonlinear simulation model to arrive at a wide-envelope simulation. Additional nonlinear terms may be included to cover complex or edge-of-the-flight-envelope maneuvers, for example, autorotation. The theoretical approach of the model stitching technique for applications to fixed-wing and rotary-wing aircraft is elaborated in chapter 17 of Ref. [2]. A thorough discussion of the method and several application examples can be found in chapters 5 and 7.7 of Ref. [6].

Model stitching is based on a set of linear state-space models at discrete flight conditions. In the case of the stitched model for the ACT/FHS, identified 11-DOF (16th order) models for five reference speeds (hover and 30, 60, 90, and 120 kt) were used, which account for blade flapping, regressive lead/lag, and mean inflow. The dimensional stability and control derivatives were extracted from these anchor point models and stored in lookup tables. Additionally, more finely spaced trim data, which capture the variation in trim states and controls over the full airspeed range, are needed. These trim data are typically first fitted with splines before being stored in lookup tables. For the ACT/FHS trim curves for the roll and pitch attitudes as well as the stick inputs were extracted from trim flights that were conducted in addition to the system identification flights. The trim points, which were extracted on a fine grid to better approximate the trim gradients, and the resulting smoothed trim curves are shown in Fig. 28.

The lookup tables are combined with the nonlinear equations of motion and other simulation elements to yield the model stitching simulation architecture. This means that known kinematic relationships such as the transformation of the gravity force into the body-fixed coordinate system, Euler attitudes, inertia, and helicopter mass are included in their nonlinear form. The linearized stitched model is identical to the original anchor point models at each of the five operating points.

One benefit of the stitching architecture is its ability to simulate maneuvering flight. Figure 29 shows the results obtained for a deceleration/acceleration maneuver that covers a wide airspeed

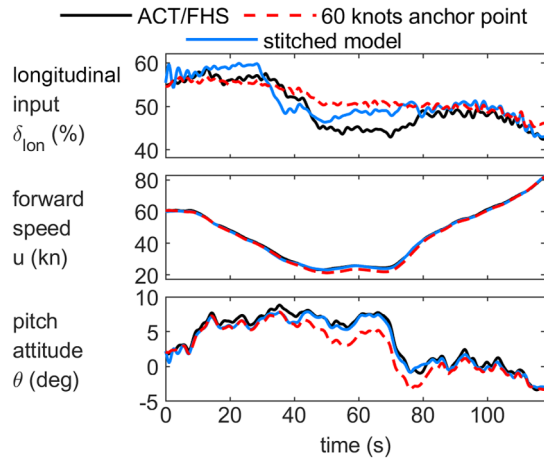


Fig. 29 Comparison of linear point model (60 kt) and stitched model for a deceleration/acceleration maneuver, from Ref. [6].

range. As the maneuver has a duration of 2 min, a flight controller minimizing attitude and speed errors is used to stabilize the unstable modes such as the phugoid. The simulated control input is the sum of the measured control and the feedback signal and therefore deviates from the measured control input. The red dashed curves show the simulated response when using the 60 kt anchor point model throughout the whole maneuver. Deviations from the measured data are most pronounced when this 60 kt model is used for small forward speeds near hover (between 50 and 80 s). The blue curves represent the stitched model. As expected, the stitched model achieves a better match of the longitudinal stick position and the pitch attitude for this maneuvering flight data.

The development of the stitched model of the ACT/FHS is described in more detail in Ref. [83]. The resulting wide-envelope model is used for flight control design and for engineering simulations at DLR. In Ref. [84], the stitched model is further improved by specially designed input filters.

VI. Other System Identification Applications

Apart from the application to fixed-wing aircraft and rotorcraft as described in the preceding sections, system identification was also applied to other flight vehicles such as gyroplanes and gliding parachutes and was used for Control Equivalent Turbulence Input (CETI) turbulence model extraction and wind field reconstruction from lidar measurements.

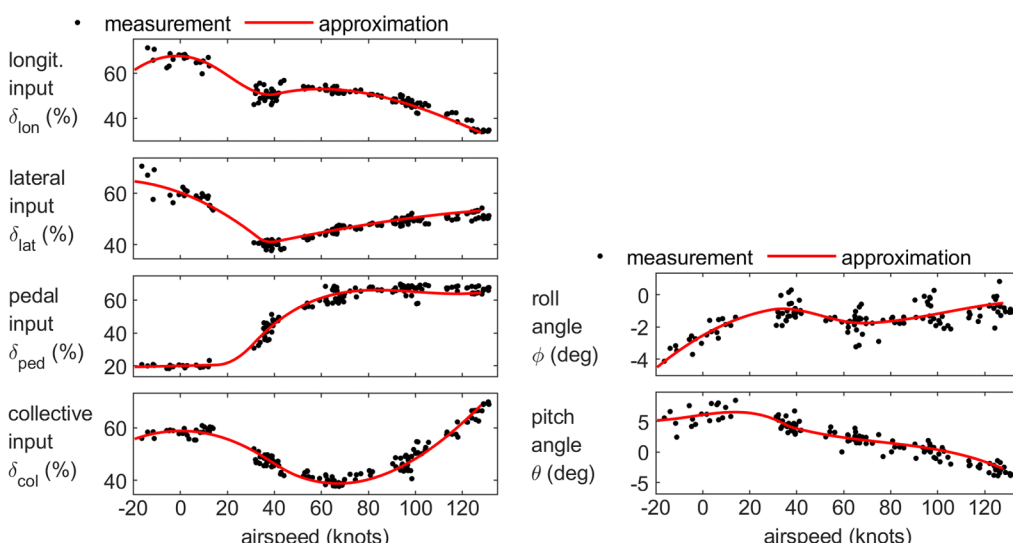


Fig. 28 Trim data of the ACT/FHS and approximated trim curves, adapted from Ref. [6].

A. Gyroplane Model

In 2008, DLR started to develop a new simulator device for gyroplane flight training [85]. A gyroplane is an ultralight flight vehicle, whose rotor is not powered directly by any mechanical device but operates in autorotation, where the power to turn the rotor results from a relative flow that is directed upward through the rotor disk. Thereby, the rotor provides lift, while forward propulsion is being provided by a propeller in pusher or tractor configuration. For this work, DLR acquired an MTOsport from AutoGyro GmbH (Fig. 30).

The gyroplane simulation model is quite comparable to standard airplane simulation models except for the fact that flight dynamics are split into a body and a rotor part. Note that the basic flight characteristics of a gyroplane are close to those of an airplane.

The body and rotor of the gyroplane are considered as a two-mass system, which is connected at the rotorhead pitch and roll pivot bolts. The rotor motion is reduced to the rotational degrees of freedom because it is assumed that, due to the lower mass of the rotor compared to the body mass, the translational motion of the rotor corresponds to that of the body. The rotor aerodynamics are calculated by a blade element method, such that the individual airflow at ten blade elements is calculated considering the rotational speed, the vertical component of the airspeed, and the flapping motion. Total aerodynamic force and moment coefficients of the gyroplane fuselage (including mast) and aerodynamic surfaces are calculated in the simulation model.

The thrust is determined depending on airspeed and propeller speed and is calculated by a combination of beam and blade element theory. Effects like crossflow, blade twist or rotation normal to the driveshaft, and the inclined flow, gyroscopic effects of the propeller and effects of the propeller wake are considered.

Eleven system identification flights were conducted in a first campaign in 2010 [85]. In a second campaign in 2012, the measurement system was supplemented with a nose boom to measure angle of attack and angle of sideslip. Flight tests consist of maneuvers to excite the gyroplane's special flight dynamics and steady-state flights at various airspeeds to determine the trim values of the gyroplane states and controls, which is necessary for a simulator model development. Level accelerations and decelerations were executed to determine the engine's characteristics. Taxi tests were conducted to identify the body drag coefficient. Additional taxi tests with pedal inputs were used to evaluate the lateral dynamics on ground and acceleration tests on ground with full throttle and at idle were performed to determine the maximum and minimum thrust as a function of the airspeed.

The output-error method in time domain was applied for the gyroplane model identification. DLR's tool FITLAB was used to estimate the unknown parameters of the simulation model implemented in MATLAB®/Simulink. Parameters of the landing gear, the propulsion, and the aerodynamic model (fuselage, rudder, stabilizer, and rotor) were estimated. Table 1 provides for example a selection of body aerodynamic parameters after system identification. As the gyroplanes lifting surface is no wing but a rotor, the aerodynamic model parameters of the body are referenced to the rotor disk area



Fig. 30 DLR's MTOsport gyroplane D-MTOS.

Table 1 Estimated body aerodynamic parameters after MTOsport system identification

Parameter	Value
Lift slope of horizontal stabilizer	$C_{La,HT}$ 5.0
Zero lift drag	C_{D0} 0.026
Angle of sideslip dependent drag	$C_{D\beta}$ 0.01
Angle of sideslip dependent side force	$C_{Y\beta}$ -0.01
Roll damping	C_{lp} -0.022
Pitch damping	C_{mq} -1.2
Weathercock stability	$C_{n\beta}$ 0.004
Rudder control efficiency	$C_{n\zeta}$ -0.010
Yaw damping	C_{nr} -0.026

instead of a reference wing. One exception is the horizontal tail parameters, which are normalized with the horizontal tail area as aerodynamic surface.

Regarding the results of the simulation model validation, a good match between flight-test data and simulation data for various maneuvers was achieved. An example of a roll doublet maneuver is provided in Fig. 31. Furthermore, an evaluation of the gyroplane's characteristics during roll on ground is given in Ref. [86].

B. Modeling of Gliding Parachutes

For precision airdrop and the recovery of space capsules, autonomous landing systems using a steerable ram-air parachute have been investigated at DLR from 1996 to 2005 [87–90]. More than 20 drop and flight tests with instrumented parafoil-payload vehicles of approximately 100 kg [named Autonomous Landing Experiment (ALEX); see Fig. 32] have been conducted in order to test guidance, navigation, and control algorithms and to obtain flight-test data for system identification and model validation. Unlike other aircraft, parachute-payload systems are highly flexible systems due to the inflated textile canopy wing and the textile lines and harnesses that connect the payload. The canopy deforms at the trailing edges as a result of control inputs, and maneuvers induce relative movements between the flexible canopy and the rigid payload. Because of the low flight velocity of such parafoil systems, their motion is greatly affected by the wind. In addition, the system is subject to large accelerations during the parachute inflation phase and at the landing impact. These untypical conditions created new challenges for instrumentation, modeling and system identification. Many of the results and lessons learned are described in Ref. [91].

Because sensors and other electronic equipment had to be selected as low-cost and robust as possible, the inaccuracies of the sensors

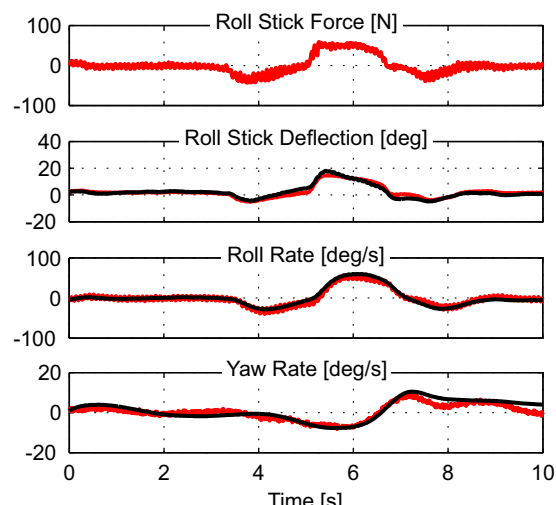


Fig. 31 Comparison of MTOsport flight-test data (red) and simulation data (black) for a roll doublet at about 30 m/s.



Fig. 32 DLR parafoil-payload system ALEX in flight.

needed correction. This problem could only partly be solved by sensor calibration. One problem was the temperature dependency especially of accelerometers, gyros, and pressure sensors. Many low-cost and MEMS sensors in the 1990s were strongly temperature sensitive and subject to self-heating but had no integrated temperature measurement or compensation. After collecting, resampling, and filtering the raw data from the flight test, a flight-path reconstruction was done to reconstruct the attitude, reduce the remaining sensor errors as much as possible, and also extract the wind influence [90,92,93].

Four different models of the parafoil-payload system have been developed, identified, and later used in simulations. The three-degree-of-freedom model considers only the CG motion (sink rate, velocity, and heading), has only four parameters, and marks the lower end of the possible flight mechanical models for the three-dimensional motion of a parafoil-load configuration. Nevertheless, the model is capable of representing some of the most important vehicle characteristics and can be used in trajectory simulations, for example, to check guidance and control functionalities. The four-degree-of-freedom model with six parameters is an extension of the three-degree-of-freedom model, taking also the roll angle into account. This model is able to simulate the increasing sink rate during turns and reproduces also the steady effects of symmetric edge deflection on the velocities and L/D . In contrast to the three-degree-of-freedom model, the reduction of forward velocity during turns is better reproduced as well. Both models are described in Ref. [92].

Because the model, for example, does not account for the distance between center of mass and the aerodynamic reference point, its capabilities are still very limited. Among others, some of the restrictions of the four-degree-of-freedom model are as follows:

- 1) The vehicle dynamic modes cannot be simulated.
- 2) Dynamic flare, caused by the load swinging forward and increasing dynamically the angle of attack, cannot be reproduced.
- 3) Aerodynamic damping in the longitudinal motion and the side force contribution to the lateral motion are neglected.
- 4) Nonlinear effect of the edge deflection is not considered.

The mentioned limitations have been solved by using a more detailed six-degree-of-freedom model that treats the full parafoil-payload system as one rigid body [94]. The aerodynamic coefficients of the parafoil canopy were initially computed by an analytical approach that considered the canopy as rigid wing with arc anhedral [95], which are then also used as starting values within a system identification [93].

Because all sensors were located in the payload, the flight-path reconstruction revealed only the motion of the payload but did not reflect the motion of the canopy, which is mainly responsible for the

aerodynamic characteristics of the vehicle. To capture the relative motion, the canopy's motion was recorded by a video camera inside the payload during the flight and evaluated afterward by image processing [96]. Provided that the evaluated relative motion between canopy and load is accurate and precisely synchronized with the data acquired in the payload, the corresponding values for the canopy can be computed by transforming the measured motion data from the payload to the canopy (Fig. 33). Using this reconstructed canopy motion, reasonable results for the aerodynamic coefficients were obtained in Refs. [93,97].

Nevertheless, the six-degree-of-freedom model still assumes a rigid body and does not include any relative motion between parafoil and payload. To overcome this limitation, a multibody approach was used for modeling the parafoil-payload system [90]. In this model, the canopy, payload, suspension lines, risers, and harness were modeled as rigid bodies that are connected via rotational joints and spring-damper elements. The full model now accounts also for relative rolling, pitching, and yawing and includes a relative shifting (or lateral displacement) mode from the parallelogramlike deformation of the harness. The model was then separated into two simplified models for longitudinal and for lateral motion that were identified separately. From these results, it could be shown that the actuator forces had a much larger influence on the relative motion than previously expected [95,98].

However, the deformations of the canopy during flight due to control line deflections and maneuvers have not explicitly been taken into account yet, or only implicitly by nonlinear control efficiencies or untypical aerodynamic coefficients. A complete understanding of the aerodynamics and flight dynamics of such a parafoil-payload system is only possible by considering the coupled fluid structure in the analysis.

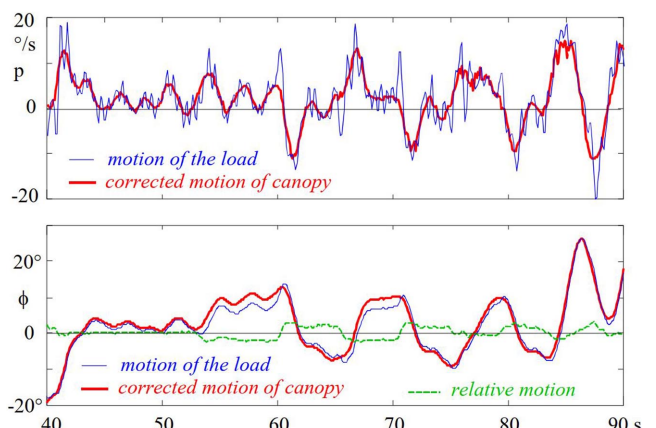


Fig. 33 Image from canopy video footage (top), payload motion, relative yawing, and corrected canopy motion (bottom), from Ref. [91].

C. CETI Turbulence Models for Rotorcraft

Empirical hover and low-speed turbulence models for rotorcraft applications have been developed using the CETI method. The CETI method was first proposed by the NRC [99] and then extensively developed at the U.S. Army [100], whereby a CETI model of the UH 60 Black Hawk helicopter was successfully developed from flight tests and validated [101].

The CETI method determines the control inputs required to generate aircraft angular and vertical rates in calm conditions that are consistent with rates observed when flying in atmospheric turbulence. The extracted CETI models are generally specific to the helicopter that was used to collect the flight data. This has the advantage that the models are automatically validated for the specific helicopter type and are therefore well suited for control system design when addressing disturbance rejection. However, in Ref. [102], a scaling method is presented that allows one to scale CETI models from one helicopter to another.

The general method for ascertaining CETI models is depicted in Fig. 34, separated into three stages; extraction, modeling, and simulation. For the *extraction* phase, data are collected from flight in turbulent conditions. The level of turbulence determines the intensity of the generated CETI model. The measured aircraft responses are then fed into an inverse aircraft model to obtain control inputs related to pilot and gusts. The quality of the final CETI model is dependent upon the quality of the inverse model used for the extraction process. Subtracting the measured pilot inputs yields equivalent control input traces that correspond to the response of the aircraft to the turbulence [100]. As shown in Ref. [103], time histories of the CETIs can either be extracted using a stable inverse model of the helicopter or by an observer approach.

In the *modeling* step, white-noise-driven transfer functions of a form similar to Dryden models are developed by analyzing the spectra of the extracted control disturbances. Therefore, the PSDs of the control equivalent inputs for each control are first generated. Each of the PSDs is then approximated by a transfer function to capture the turbulence characteristics of the corresponding axis. For a standard helicopter, this modeling process yields four transfer function filters, one for each control input.

When using the CETI model for *simulation*, white noise is passed through these transfer function filters to generate control equivalent turbulence inputs. These are added to the pilot inputs, sending a combined disturbance to the vehicle swashplate.

The CETI method was first applied at DLR using the ACT/FHS in hover [103,104]. More recently, the use of the method was extended to forward flight, resulting in a CETI model that covers most of the envelope [105,106]. The extraction of the CETIs was performed using the inverse model approach based on high-fidelity identified models as described in Ref. [77].

The same model structure as used in the hover case was also applied for the turbulence models in forward flight, namely,

$$G_{\text{lon}} = \frac{\delta_{\text{lon,CETI}}}{W_{\text{noise}}} = A_{\text{lon}} \frac{1}{(s + (U_0/L_w))} \quad (25)$$

$$G_{\text{lat}} = \frac{\delta_{\text{lat,CETI}}}{W_{\text{noise}}} = A_{\text{lat}} \frac{1}{(s + (U_0/L_w))} \quad (26)$$

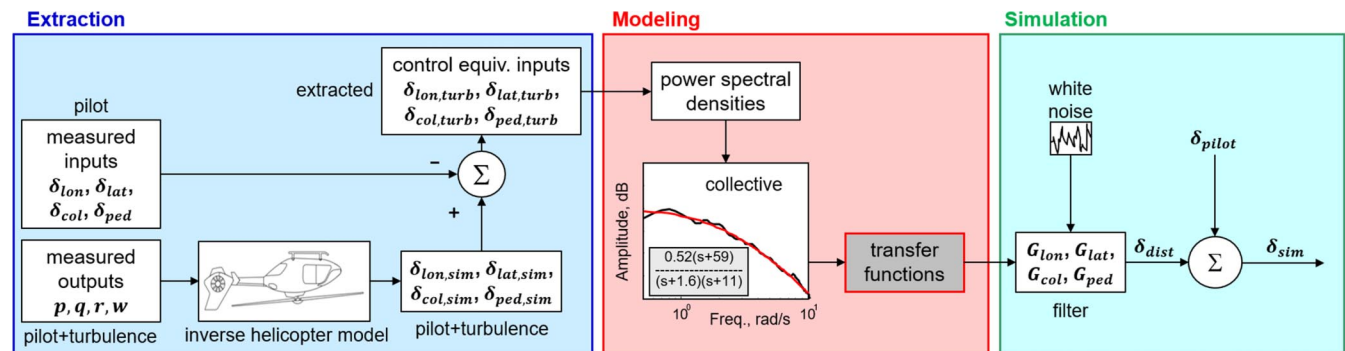


Fig. 34 CETI method, from Ref. [105].

$$G_{\text{ped}} = \frac{\delta_{\text{ped,CETI}}}{W_{\text{noise}}} = A_{\text{ped}} \frac{1}{(s + (U_0/L_v))} \quad (27)$$

$$G_{\text{col}} = \frac{\delta_{\text{col,CETI}}}{W_{\text{noise}}} = A_{\text{col}} \frac{(s + 20(U_0/L_w))}{(s + f_{p1}(U_0/L_w))(s + 5(U_0/L_w))} \quad (28)$$

The model consists of first-order transfer functions for longitudinal, lateral, and pedal inputs and a second-order transfer function for the vertical axis (collective inputs). The transfer functions for longitudinal and lateral control have the same denominator (depending on U_0/L_w , the quotient between mean wind speed and main rotor scaling length) and only different amplitudes ($A_{\text{lon}}, A_{\text{lat}}$). The transfer function for pedal inputs has the same structure but uses the tail rotor scaling length L_v instead of L_w . The transfer function for collective is coupled to those for longitudinal and lateral inputs by U_0/L_w . In the turbulence models for hover determined in Ref. [103], the factor f_{p1} in the transfer function for collective was set as a constant parameter, equal to 0.63. However, this value is valid only for hover, and it was required to vary this parameter for forward flight.

Turbulence models were first identified separately for the different reference speeds (hover and 30, 60, and 90 kt). Figure 35 shows the spectra (PSDs) and the identified model for 60 kt. The extracted CETI data could be grouped into three distinct turbulence levels (low, medium, and high), and the identified model describes the data well.

The individual turbulence models were identified using FITLAB to approximate the PSDs (as frequency responses) by transfer functions. The identified model parameters were then plotted as functions of turbulence intensity and speed. To arrive at a model that can be smoothly interpolated between the speeds, two parameters of the 30 kt models were adjusted, and the remaining model parameters for these cases were reiterated. This provided an overall model with only a slight degradation in model quality for these modified cases.

The corresponding results are shown in Fig. 36. It can be seen that smooth surfaces were obtained for all parameters. The factor f_{p1} is equal to 0.63 at hover and reduced with forward speed. All amplitude parameters except for A_{lat} increase with speed, and the amplitudes at the highest turbulence intensity level are larger than those for the lowest level by a factor of 2–3.

The identified models were implemented and successfully tested through piloted simulations in the AVES motion-base platform as described in Ref. [106].

D. Wind Field Reconstruction from Airborne Lidar Measurements

The development of more efficient aircraft is a key element in continuing efforts to improve the sustainability of aviation. Through the design of active load alleviation systems, the load envelope can be shrunk, and weight savings might be obtained. Achieving large levels of load alleviation for external disturbances, especially gusts, is challenging because gust load alleviation systems have only little time to react to gusts. Pitching commands are very effective, but the entire aircraft has to rotate first, which is hardly possible with only the lead time of in situ air data measurements on the aircraft nose. A solution would be to measure the gusts slightly in advance. This requires remote wind sensing technologies, like Doppler wind lidar

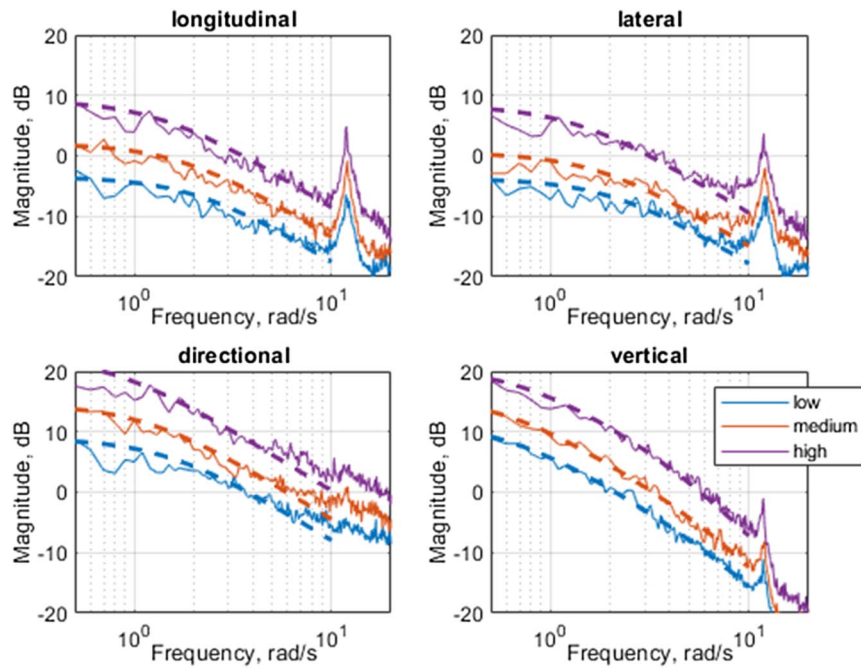


Fig. 35 PSDs and extracted turbulence model (60 kt; solid: PSD; dashed: model), from Ref. [105].

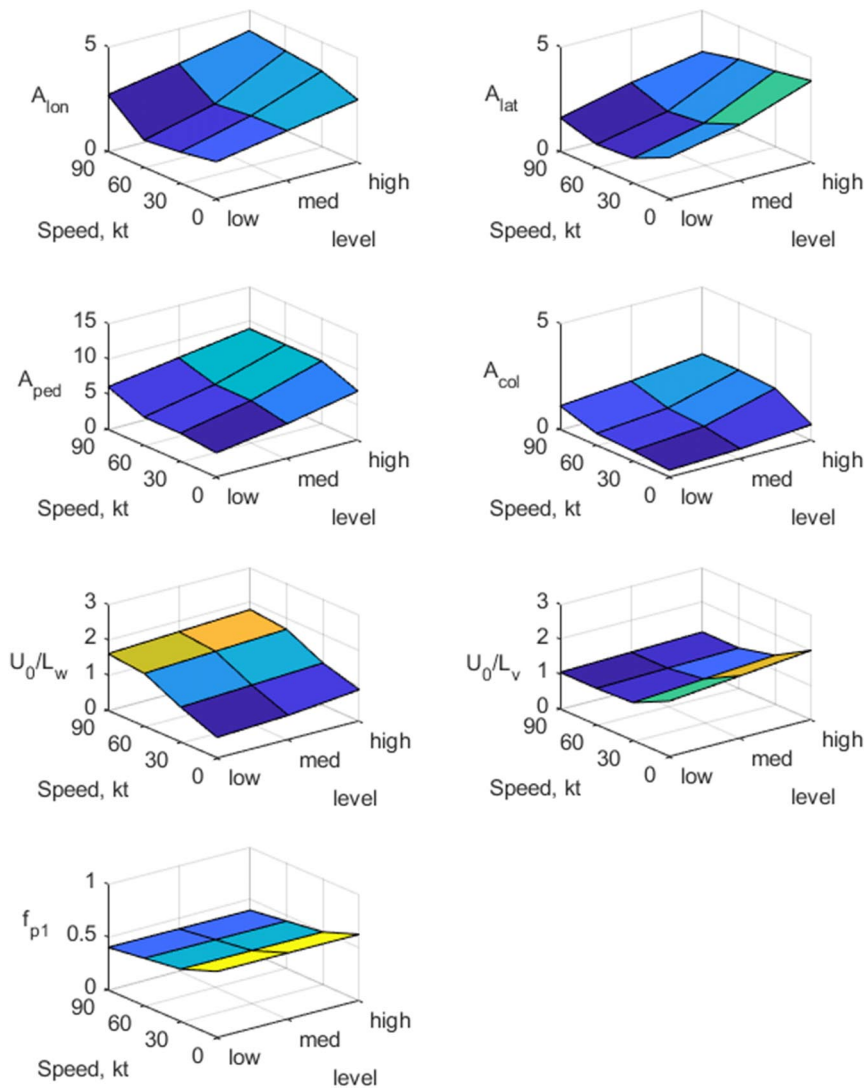


Fig. 36 Model parameters vs speed and turbulence level, from Ref. [105].

sensors. A major issue is that these sensors only measure the relative wind component in the direction of the laser beam (so-called line-of-sight direction). In addition, the line-of-sight speed measurements are very noisy.

An online identification process is needed to interpret the numerous raw lidar speed measurements and estimate the transversal (vertical and lateral) wind components in the vicinity of the aircraft. Despite the noisy line-of-sight speed measurements, a good estimation of the wind field is possible because of the very large number of measurements. For example, with a laser pulse repetition frequency of 500 Hz and nine measurements along the line-of-sight per pulse, 4500 speed measurements are obtained per second. Figure 37 illustrates the wind field estimation process from airborne lidar line-of-sight speed measurements [107]. The resulting wind field model consists of wind velocity components at evenly spaced nodes parameterized by a lead time τ_{lead} and a lag time τ_{lag} . Mathematically, the wind reconstruction is a maximum likelihood problem; it determines the wind velocities at the estimation mesh nodes which yield the optimal fit (in the least-squares sense) to the obtained line-of-sight speed measurements z_i . Each measurement is weighted by the inverse of its corresponding standard deviation σ_i to account for the difference in noise levels of each measurement (e.g., depending on local atmospheric conditions and measurement range). The simplest implementation is a sole vertical wind profile as represented in Fig. 37, but the same kind of model can be used in two or three dimensions (both for node locations and for wind components at each node).

Additionally, a Tikhonov regularization is included in the optimization problem to ensure a certain degree of smoothness in the resulting estimated wind field. The matrix Γ_1 penalizes the first spatial derivative of the wind field, and Γ_2 penalizes its second spatial derivative. This regularization can also be seen (and mathematically formulated) as a priori information on the wind field. These terms express the fact that the very small-scale turbulence is not interesting for load alleviation and that these small scales are unlikely to be found

in the lidar measurements, not because they are not present in the volume of air scanned by the sensor but rather due to the sensor's limited spatial resolution. The scalar coefficients γ_1 and γ_2 enable tuning the relative weight between the Tikhonov regularization terms and the least-squares criterion.

After a few transformations, the regularized optimization problem, with two Tikhonov terms, reads

$$\hat{\boldsymbol{\theta}} = \arg \min_{\boldsymbol{\theta}} \left(\sum_{i=1}^N \frac{(z_i - y_i(\boldsymbol{\theta}))^2}{\sigma_i^2} + \gamma_1 \|\boldsymbol{\Gamma}_1 \boldsymbol{\theta}\|^2 + \gamma_2 \|\boldsymbol{\Gamma}_2 \boldsymbol{\theta}\|^2 \right) \quad (29)$$

In this specific case, the p parameters in $\boldsymbol{\theta}$ correspond to the individual wind velocity components at the model nodes. When used for a series of nodes along the flight path, as in Fig. 37, the Tikhonov regularization matrices $\boldsymbol{\Gamma}_1$ and $\boldsymbol{\Gamma}_2$ are, respectively, of sizes $(p-1) \times p$ and $(p-2) \times p$. More detailed explanations on the wind field estimation problem from lidar line-of-sight speed measurements, its solution, and how this information can be used by gust load alleviation controllers are given in Refs. [107–111].

Another application based on onboard lidar measurements is the identification of wake vortices [107,112,113] shortly before encountering them with the aim of mitigating their impact [114–116]. As pointed out in Ref. [107], the identification of wake vortices from lidar measurements is very similar to detecting gusts and turbulence. The parametric models of wake vortices yield a lower number of parameters (the circulation as main parameter for the vortex strength and geometrical parameters position and orientation, possibly deformations). The relationships between the parameters and the model outputs (predicted line-of-sight velocity measurements) is, however, strongly nonlinear, and the identification of the vortices is therefore more challenging than in the aforementioned gust/turbulence case.

Multiple starting values are used and different strategies have been developed to robustify the convergence of the algorithm. Another way to drastically improve the identification procedure is to optimize

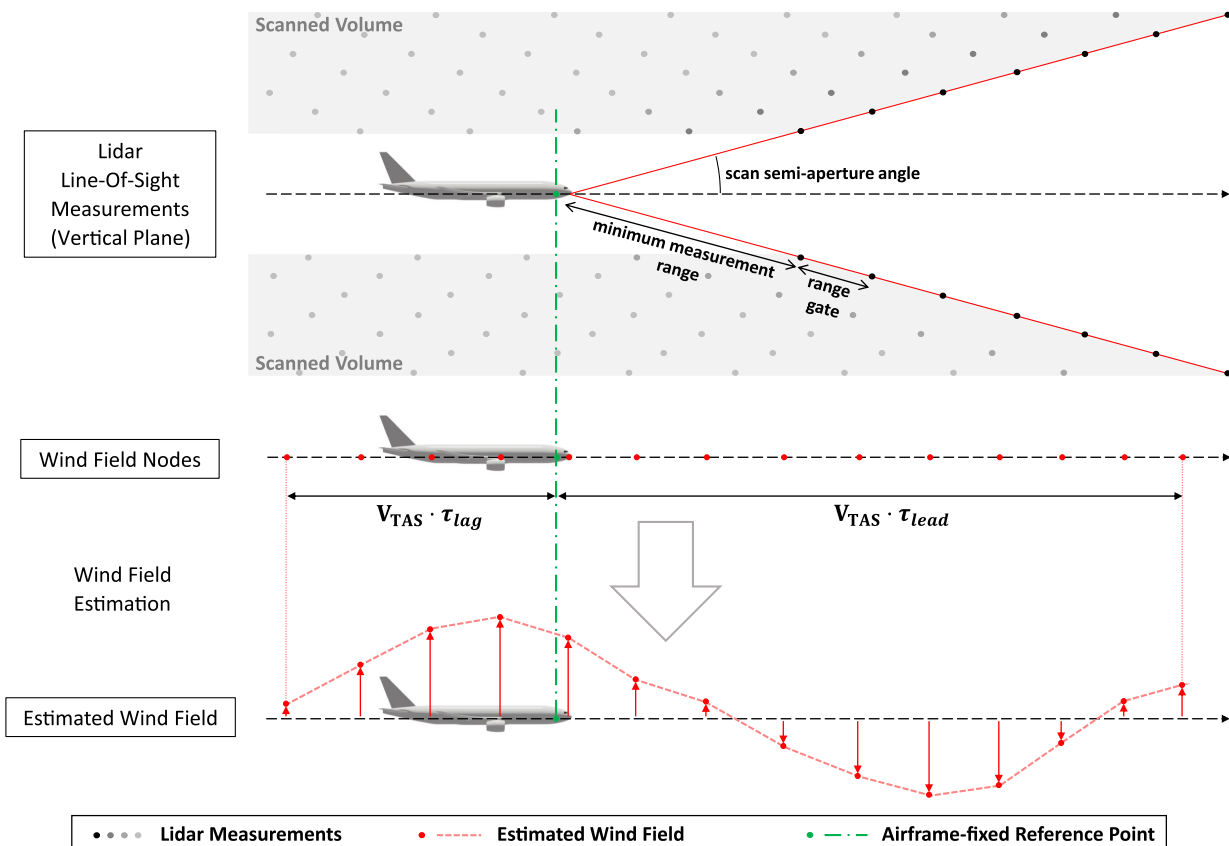


Fig. 37 Illustration of wind estimation process: from lidar line-of-sight speed measurements to estimated wind field (in vertical direction), adapted from Ref. [108].

the set of measurements used for the identification by optimizing the scan geometry [117,118].

VII. Conclusions

This paper provides an overview of applications of system identification at DLR in recent years.

The well-established system identification tools developed by DLR over the years have been further improved and supplemented by new methodologies and toolboxes, such as the identification of blackbox models, which provide fidelity comparable to that of high-order physics-based models. The optimization of flight test is a major task, as a reduction of the flight time required for system identification maneuvers can reduce costs significantly. Therefore, new methods to generate specific excitation maneuvers were developed. The model identification with the data obtained using the newly developed maneuvers showed very promising results.

Several applications of system identification on fixed-wing aircraft have further provided very interesting and notable results. Within a dedicated process to analyze operational flight data, an engine thrust model was derived using a combination of fundamental engineering knowledge, parameter estimation techniques, and big data methods. The specific effects of airframe icing can be described and identified with an additive Δ -model to the basic aircraft simulation. It was also shown that, with a sufficient number of accelerometers and strain gauges distributed over the aircraft, it is possible to identify flexible aircraft models with the gathered data. Additionally, a specific flexible sailplane model for loads monitoring was identified from flight and on-ground static calibration data.

In rotorcraft system identification, the extension of the model validity to higher frequencies was possible by accounting for the rotor degrees of freedom in the models. It was also shown that including engine dynamics further improves the model quality. Moreover, even without additional sensor installation on the helicopter, the tailboom vertical bending mode could be successfully identified. A rotor-state observer was developed using identified models that match the measured rotor mast moments. Applying model stitching techniques allowed merging models identified at different reference conditions into a wide-envelope simulation environment.

One major purpose of system identification in aeronautics is the development of simulator models for training. Specific research on the modeling and identification of gyroplanes faced the challenges of their unconventional flight characteristics and resulted in a high-quality simulation model for pilot training. Furthermore, several gliding parachute models with different model fidelity have been identified from flight-test data, and it was shown that several factors are influencing the complex dynamics of the coupled parachute-payload system.

Aside from vehicle identification, additional work was done in the field of modeling atmospheric disturbances. CETI turbulence models for the ACT/FHS rotorcraft were derived and successfully implemented and tested in DLR's AVES simulation. Using lidar line-of-sight speed measurements, the wind field in the vicinity of an aircraft was estimated. This application can be used for load alleviation or to counteract wake vortices.

The wide variety of applications presented shows that flight vehicle system identification is a highly powerful, useful, and indispensable tool.

Acknowledgments

The authors want to thank most sincerely their current and former colleagues from the DLR Institute of Flight Systems for their outstanding research work described and cited in this paper. Moreover, a special thank goes to the following colleagues for their specific contributions to this paper on certain topics: Insa Pruter (gyroplane model), Thomas Jann (modeling of gliding parachutes), and Nicolas Fezans (wind field reconstruction from airborne lidar measurements).

References

- [1] Jategaonkar, R. V., *Flight Vehicle System Identification—A Time Domain Methodology*, 2nd ed., Progress in Astronautics and Aeronautics, Vol. 245, AIAA, Reston, VA, 2015.
- [2] Tischler, M. B., and Remple, R. K., *Aircraft and Rotorcraft System Identification: Engineering Methods with Flight-Test Examples*, 2nd ed., AIAA Education Series, AIAA, Reston, VA, 2012.
- [3] Klein, V., and Morelli, E. A., *Aircraft System Identification—Theory and Practice*, AIAA Education Series, AIAA, Reston, VA, 2006.
- [4] Hamel, P. G., and Jategaonkar, R. V., "Evolution of Flight Vehicle System Identification," *Journal of Aircraft*, Vol. 33, No. 1, 1996, pp. 9–28.
<https://doi.org/10.2514/3.46898>
- [5] Hamel, P. G., and Kaletka, J., "Advances in Rotorcraft System Identification," *Progress in Aerospace Sciences*, Vol. 33, Nos. 3–4, 1997, pp. 259–284.
[https://doi.org/10.1016/S0376-0421\(96\)00005-X](https://doi.org/10.1016/S0376-0421(96)00005-X)
- [6] Tischler, M. B., White, M. D., Jones, M., Scepanovic, P., Seher-Weiß, S., Myrand-Lapierre, V., Nadeau-Beaulieu, M., Richard, S., Ragazzi, A., D'Agosto, S., He, C., Lehman, R., Miller, D., Xin, H., Gubbels, A., Hui, K., Taghizad, A., Tobias, E., Greiser, S., Pavel, M., Stroosma, O., Yavruçuk, I., Padfield, G. D., Cameron, N., Prasad, J., Guner, F., Juhasz, O., Horn, J., Soong, J., Nadell, S., and Lee, O., "Rotorcraft Flight Simulation Model Fidelity Improvement and Assessment," NATO STO-TR-AVT-296-UU, Neuilly-sur-Seine, France, May 2021.
<https://doi.org/10.14339/STO-TR-AVT-296-UU>
- [7] Jategaonkar, R. V., Fischenberg, D., and von Grünhagen, W., "Aero-dynamic Modeling and System Identification from Flight Data—Recent Applications at DLR," *Journal of Aircraft*, Vol. 41, No. 4, 2004, pp. 681–691.
<https://doi.org/10.2514/1.3165>
- [8] Von Grünhagen, W., Schönenberg, T., Lantzsch, R., Lusardi, J. A., Lee, D., and Fischer, H., "Handling Qualities Studies into the Interaction Between Active Sidestick Parameters and Helicopter Response Types," *CEAS Aeronautical Journal*, Vol. 5, No. 1, 2014, pp. 13–28.
<https://doi.org/10.1007/s13272-013-0079-7>
- [9] Greiser, S., Lantzsch, R., Wolfram, J., Wartmann, J., Mühlhäuser, M., Lüken, T., Döhler, H.-U., and Peinecke, N., "Results of the Pilot Assistance System—Assisted Low-Level Flight and Landing on Unprepared Landing Sites—Obtained with the ACT/FHS Research Rotorcraft," *Aerospace Science and Technology*, Vol. 45, Sept. 2015, pp. 215–227.
<https://doi.org/10.1016/j.ast.2015.05.017>
- [10] Kim, H.-M., Nonnenmacher, D., Götz, J., Weber, P., von Hinüber, E., and Knedlik, S., "Initial Flight Tests of an Automatic Slung Load Control System for the ACT/FHS," *CEAS Aeronautical Journal*, Vol. 7, No. 2, 2016, pp. 209–224.
<https://doi.org/10.1007/s13272-016-0181-8>
- [11] Kaletka, J., Kurscheid, H., and Butter, U., "FHS, the New Research Helicopter: Ready for Service," *Aerospace Science and Technology*, Vol. 9, No. 5, 2005, pp. 456–467.
<https://doi.org/10.1016/j.ast.2005.02.003>
- [12] Duda, H., Gerlach, T., Advani, S. K., and Potter, M., "Design of the DLR AVES Research Flight Simulator," *AIAA Modeling and Simulation Technologies (MST) Conference*, AIAA Paper 2013-4737, 2013.
<https://doi.org/10.2514/6.2013-4737>
- [13] Seher-Weiss, S., "FitlabGui—A Versatile Tool for Data Analysis, System Identification and Helicopter Handling Qualities Analysis," *42nd European Rotorcraft Forum*, Lille, France, 2016, Paper 29, <http://hdl.handle.net/20.500.11881/3737> [retrieved 26 March 2023].
- [14] USAF MIL-STD-1797B, "Flying Qualities of Piloted Aircraft," Dept. of Defense Interface Standard, 2006.
- [15] Wartmann, J., and Greiser, S., "Identification and Selection of Rotorcraft Candidate Models to Predict Handling Qualities and Dynamic Stability," *44th European Rotorcraft Forum*, Delft, The Netherlands, 2018, Paper 30, <http://hdl.handle.net/20.500.11881/3944> [retrieved 26 March 2023].
- [16] Wartmann, J., "ACT/FHS System Identification Including Engine Torque and Main Rotor Speed Using the PBSIDopt Method," *41st European Rotorcraft Forum*, Munich, Germany, 2015, Paper 16, <http://hdl.handle.net/20.500.11881/3535> [retrieved 26 March 2023].
- [17] Chiuso, A., "The Role of Vector Autoregressive Modeling in Predictor-Based Subspace Identification," *Automatica*, Vol. 43, No. 6, 2007, pp. 1034–1048.
<https://doi.org/10.1016/j.automatica.2006.12.009>
- [18] Chiuso, A., "On the Relation Between CCA and Predictor-Based Subspace Identification," *IEEE Transactions on Automatic Control*,

- Vol. 52, No. 10, 2007, pp. 1795–1812.
<https://doi.org/10.1109/TAC.2007.906159>
- [19] Chiuso, A., “On the Asymptotic Properties of Closed-Loop CCA-Type Subspace Algorithms: Equivalence Results and Role of the Future Horizon,” *IEEE Transactions on Automatic Control*, Vol. 55, No. 3, 2010, pp. 634–649.
<https://doi.org/10.1109/TAC.2009.2039239>
- [20] Van der Veen, G., van Wingerden, J.-W., Bergamasco, M., Lovera, M., and Verhaegen, M., “Closed-Loop Subspace Identification Methods: An Overview,” *IET Control Theory & Applications*, Vol. 7, No. 10, 2013, pp. 1339–1358.
<https://doi.org/10.1049/iet-cta.2012.0653>
- [21] Scher-Weiß, S., and Wartmann, J., “Initial Investigation into the Complementary Use of Black Box and Physics-Based Techniques in Rotorcraft System Identification,” *CEAS Aeronautical Journal*, Vol. 11, No. 2, 2020, pp. 501–513.
<https://doi.org/10.1007/s13272-019-00431-z>
- [22] Baskett, B. J., Aeronautical Design Standard, Performance Specification, Handling Qualities Requirements for Military Rotorcraft, U.S. Army Aviation and Missile Command, Aviation Engineering Directorate, Redstone Arsenal, ADS-33E-PRF, 2000, <https://apps.dtic.mil/sti/citations/ADA515904> [retrieved 26 March 2023].
- [23] Blanken, C. L., Tischler, M. B., Lusardi, J. A., Ivler, C. M., and Lehmann, R., *Proposed Revisions To Aeronautical Design Standard—33E (ADS-33E-PRF) TOWARD ADS-33F-PRF*, U.S. Army Combat Capabilities Developemt Command Aviation & Missile Center, 2019, <https://apps.dtic.mil/sti/citations/AD1080657> [retrieved 26 March 2023].
- [24] Jategaonkar, R. V., and Thielecke, F., “ESTIMA—An Integrated Software Tool for Nonlinear Parameter Estimation,” *Aerospace Science and Technology*, Vol. 6, No. 8, 2002, pp. 565–578.
[https://doi.org/10.1016/S1270-9638\(01\)01143-9](https://doi.org/10.1016/S1270-9638(01)01143-9)
- [25] Raab, C., “Rapid Aerodynamic Parameter Identification on a Large Transport Aircraft,” *AIAA Atmospheric Flight Mechanics Conference at SciTech*, AIAA Paper 2014-0730, 2014.
<https://doi.org/10.2514/6.2014-0730>
- [26] Morelli, E., “Real-Time Parameter Estimation in the Frequency Domain,” *Journal of Guidance, Navigation and Control*, Vol. 23, No. 5, 2000, pp. 812–818.
<https://doi.org/10.2514/2.4642>
- [27] Deiler, C., “Data Parser Approaches for (online) Parameter Estimation,” *CEAS Aeronautical Journal*, Vol. 5, No. 3, 2014, pp. 345–357.
<https://doi.org/10.1007/s13272-014-0110-7>
- [28] Raab, C., Ohme, P., and Deiler, C., “Support of Icing Flight Tests by Near Real-Time Data Analysis,” *CEAS Aeronautical Journal*, Vol. 8, No. 4, 2017, pp. 561–577.
<https://doi.org/10.1007/s13272-017-0260-5>
- [29] Deiler, C., and Fezans, N., “VIRTTAC—A Family of Virtual Test Aircraft for Use in Flight Mechanics and GNC Benchmarks,” *AIAA SciTech 2019 Forum*, AIAA Paper 2019-0950, 2019.
<https://doi.org/10.2514/6.2019-0950>
- [30] Fezans, N., Deiler, C., and Roeser, M. S., “Generation of a Dataset for System Identification with VIRTTAC-Castor,” *German Aerospace Conference (DLRK)*, Deutsche Gesellschaft für Luft- und Raumfahrt (DGLR), Darmstadt, Germany, 2019, <https://elib.dlr.de/129105/> [retrieved 26 March 2023].
- [31] Roeser, M. S., “Multi-Axis Maneuver Design for Aircraft Parameter Estimation,” *German Aerospace Conference (DLRK)*, Deutsche Gesellschaft für Luft- und Raumfahrt, Friedrichshafen, Germany, 2018, <https://elib.dlr.de/121687/> [retrieved 26 March 2023].
- [32] Roeser, M. S., and Fezans, N., “Method for Designing Multi-Input System Identification Signals Using a Compact Time-Frequency Representation,” *CEAS Aeronautical Journal*, Vol. 12, No. 2, 2021, pp. 291–306.
<https://doi.org/10.1007/s13272-021-00499-6>
- [33] Mallat, S., *A Wavelet Tour of Signal Processing—The Sparse Way*, 3rd ed., Academic Press, Burlington, MA, 2008.
- [34] Lichota, P., Sibilski, K., and Ohme, P., “D-Optimal Simultaneous Multistep Excitations for Aircraft Parameter Estimation,” *Journal of Aircraft*, Vol. 54, No. 2, 2017, pp. 747–758.
<https://doi.org/10.2514/1.C033794>
- [35] Berger, T., Tischler, M. B., Knapp, M. E., and Lopez, M. J. S., “Identification of Multi-Input Systems in the Presence of Highly Correlated Inputs,” *Journal of Guidance, Control, and Dynamics*, Vol. 41, No. 10, 2018, pp. 2247–2257.
<https://doi.org/10.2514/1.G003530>
- [36] Morelli, E. A., “Multiple Input Design for Real-Time Parameter Estimation in the Frequency Domain,” *IFAC Proceedings Volumes*, Vol. 36, No. 16, 2003, pp. 639–644.
[https://doi.org/10.1016/S1474-6670\(17\)34833-4](https://doi.org/10.1016/S1474-6670(17)34833-4)
- [37] Tulleken, H. J. A. F., “Generalized Binary Noise Test-Signal Concept for Improved Identification-Experiment Design,” *Automatica*, Vol. 26, No. 1, 1990, pp. 37–49.
[https://doi.org/10.1016/0005-1098\(90\)90156-C](https://doi.org/10.1016/0005-1098(90)90156-C)
- [38] Chen, J.-K., and Yu, C.-C., “Optimal Input Design Using Generalized Binary Sequence,” *Automatica*, Vol. 33, No. 11, 1997, pp. 2081–2084.
[https://doi.org/10.1016/S0005-1098\(97\)00122-2](https://doi.org/10.1016/S0005-1098(97)00122-2)
- [39] Wartmann, J., “Closed-Loop Rotorcraft System Identification Using Generalized Binary Noise,” *AHS International 73rd Annual Forum & Technology Display*, American Helicopter Soc. Paper 104, Fort Worth, TX, 2017.
- [40] Breeman, J. H., “Flight Test Data Quality Evaluation,” *Rotorcraft System Identification*, AGARD Advisory Rept. AR 280, 1991.
- [41] Mulder, J. A., Chu, Q. P., Sridhar, J. K., Breeman, J. H., and Laban, M., “Non-Linear Aircraft Flight Path Reconstruction Review and New Advances,” *Progress in Aerospace Sciences*, Vol. 35, No. 7, 1999, pp. 673–726.
[https://doi.org/10.1016/S0376-0421\(99\)00005-6](https://doi.org/10.1016/S0376-0421(99)00005-6)
- [42] Teixeira, B. O., Törres, L. A., Iscold, P., and Aguirre, L. A., “Flight Path Reconstruction—A Comparison of Nonlinear Kalman Filter and Smoother Algorithms,” *Aerospace Science and Technology*, Vol. 15, No. 1, 2011, pp. 60–71.
<https://doi.org/10.1016/j.ast.2010.07.005>
- [43] Julier, S. J., and Uhlmann, J. K., “A New Extension of the Kalman Filter to Nonlinear Systems,” *AeroSense: The 11th International Symposium on Aerospace/Defence Sensing, Simulation and Controls*, International Soc. for Optics and Photonics (SPIE), Bellingham, WA, 1997, pp. 182–193.
<https://doi.org/10.1117/12.280797>
- [44] Van der Merwe, R., and Wan, E. A., “The Square-Root Unscented Kalman Filter for State and Parameter-Estimation,” *IEEE International Conference on Acoustics, Speech, and Signal Processing*, IEEE, New York, 2001, pp. 4555–4559.
<https://doi.org/10.1109/ICASSP.2001.940586>
- [45] Julier, S. J., “The Scaled Unscented Transformation,” *Proceedings of the American Control Conference*, Vol. 6, IEEE, New York, 2002, pp. 3461–3464.
<https://doi.org/10.1109/ACC.2002.1025369>
- [46] Wartmann, J., Wolfram, J., and Gestwa, M., “Sensor Fusion and Flight Path Reconstruction of the ACT/FHS Rotorcraft,” *CEAS Aeronautical Journal*, Vol. 6, No. 4, 2015, pp. 529–539.
<https://doi.org/10.1007/s13272-015-0162-3>
- [47] Särkkä, S., “Unscented Rauch-Tung-Striebel Smoother,” *IEEE Transactions on Automatic Control*, Vol. 53, No. 3, 2008, pp. 845–849.
<https://doi.org/10.1109/TAC.2008.919531>
- [48] Tikhonov, A. N., John, F., and Arsenin, V., *Solutions of Ill-Posed Problems*, Halsted Press Book, V.H. Winston & Sons, Washington, D.C., 1977.
- [49] Tikhonov, A. N., Goncharsky, A. V., Stepanov, V., and Yagola, A., *Numerical Methods for the Solution of Ill-Posed Problems*, Mathematics and Its Applications, Springer, Dordrecht, The Netherlands, 1995.
<https://doi.org/10.1007/978-94-015-8480-7>
- [50] Deiler, C., “Engine Thrust Model Determination from Large Operational Flight Data Base,” *6th CEAS Conference on Guidance, Navigation and Control (EuroGNC)*, Council of European Aerospace Societies (CEAS), Berlin, 2022.
- [51] Deiler, C., “Engine Thrust Model Determination and Analysis Using a Large Operational Flight Database,” *CEAS Aeronautical Journal*, Vol. 14, No. 1, 2022, pp. 29–45.
<https://doi.org/10.1007/s13272-022-00625-y>
- [52] N. N., *Certification Specifications and Acceptable Means of Compliance for Large Aeroplanes CS-25, Amendment 16*, European Aviation Safety Agency (EASA), Cologne, Germany, March 2015.
- [53] N. N., *Federal Regulation Title 14.I.C Part 25—Airworthiness Standards: Transport Category Airplanes*, Federal Aviation Administration, Nov. 2014.
- [54] Deiler, C., and Kilian, T., “Dynamic Aircraft Simulation Model Covering Local Icing Effects,” *CEAS Aeronautical Journal*, Vol. 9, No. 3, 2018, pp. 429–444.
<https://doi.org/10.1007/s13272-018-0291-6>
- [55] Deiler, C., “Comparison of Flight Characteristics of Two Different Airplanes and Ice Configurations,” *Journal of Aircraft*, Vol. 57, No. 5, 2020, pp. 995–1000.
<https://doi.org/10.2514/1.C035801>
- [56] Deiler, C., “Time Domain Output Error System Identification of Iced Aircraft Aerodynamics,” *CEAS Aeronautical Journal*, Vol. 8, No. 2,

- 2017, pp. 231–244.
<https://doi.org/10.1007/s13272-016-0231-2>
- [57] Deiler, C., “Aerodynamic Modeling, System Identification, and Analysis of Iced Aircraft Configurations,” *Journal of Aircraft*, Vol. 55, No. 1, 2018, pp. 145–161.
<https://doi.org/10.2514/1.C034390>
- [58] Deiler, C., Ohme, P., Raab, C., Mendonca, C., and Silva, D., “Facing the Challenges of Supercooled Large Droplet Icing: Results of a Flight Test Based Joint DLR-Embraer Research Project,” *SAE International Journal of Advances and Current Practices in Mobility*, Vol. 2, No. 1, 2020, pp. 192–204.
<https://doi.org/10.4271/2019-01-1988>
- [59] Deiler, C., “Flight Characteristics with Different Supercooled Large Droplet Ice Configurations,” *Aeronautical Journal*, Vol. 126, No. 1299, 2021, pp. 848–865.
<https://doi.org/10.1017/aer.2021.98>
- [60] Deiler, C., and Fezans, N., “Performance-Based Ice Detection Methodology,” *Journal of Aircraft*, Vol. 57, No. 2, 2020, pp. 209–223.
<https://doi.org/10.2514/1.C034828>
- [61] Waszak, M. R., and Schmidt, D. K., “Flight Dynamics of Aeroelastic Vehicles,” *Journal of Aircraft*, Vol. 25, No. 6, 1988, pp. 563–571.
<https://doi.org/10.2514/3.45623>
- [62] De Oliveira Silva, B. G., and Mönnich, W., “System Identification of Flexible Aircraft in Time Domain,” *AIAA Atmospheric Flight Mechanics Conference*, AIAA Paper 2012-4412, 2012.
<https://doi.org/10.2514/6.2012-4412>
- [63] De Oliveira Silva, B. G., “Data Gathering and Preliminary Results of the System Identification of a Flexible Aircraft Model,” *AIAA Atmospheric Flight Mechanics Conference*, AIAA Paper 2011-6355, 2011.
<https://doi.org/10.2514/6.2011-6355>
- [64] De Oliveira Silva, B. G., “System Identification of Flexible Aircraft in Time Domain,” Ph.D. Thesis, DLR-FB-2018-29, TU Braunschweig, Braunschweig, Germany, 2018, <https://elib.dlr.de/124432/> [retrieved 26 March 2023].
- [65] Preisighe Viana, M. V., “Sensor Calibration for Calculation of Loads on a Flexible Aircraft,” *International Forum on Aeroelasticity and Structural Dynamics (IFASD)*, Central Aerohydrodynamic Institute (TsAGI), in collaboration with the CEAS and the AIAA, Saint Petersburg, Russia, Paper 42, 2015, elib.dlr.de/97681/1/IFASD2015_042_Marcus%20Vinicius%20P.%20Viana_Final.pdf [retrieved 26 March 2023].
- [66] Mönnich, W., “Ein 2-Punkt-Aerodynamikmodell für die Identifizierung,” *Symposium “Systemidentifizierung in der Fahrzeugdynamik”*, Paper No. 3.1 in DFVLR-Mitteilung 87-22, 1987 (in German).
- [67] Preisighe Viana, M. V., “Time-Domain System Identification of Rigid-Body Multipoint Loads Model,” *AIAA Atmospheric Flight Mechanics Conference at Aviation*, AIAA Paper 2016-3706, 2016.
<https://doi.org/10.2514/6.2016-3706>
- [68] Klimmek, T., Ohme, P., Ciampa, P. D., and Handojo, V., “Aircraft Loads—An Important Task from Pre-Design to Loads Flight Testing,” *German Aerospace Conference (DLRK)*, Deutsche Gesellschaft für Luft- und Raumfahrt, 2016, Paper 420223, www.dglr.de/publikationen/2017/420223.pdf [retrieved 26 March 2023].
- [69] Raab, C., and Rohde-Brandenburger, K., “In-Flight Testing of MEMS Pressure Sensors for Flight Loads Determination,” *AIAA Atmospheric Flight Mechanics Conference at SciTech*, AIAA Paper 2020-0512, 2020.
<https://doi.org/10.2514/6.2020-0512>
- [70] Raab, C., and Rohde-Brandenburger, K., “Dynamic Flight Load Measurements with MEMS Pressure Sensors,” *CEAS Aeronautical Journal*, Vol. 12, No. 4, 2021, pp. 737–753.
<https://doi.org/10.1007/s13272-021-00529-3>
- [71] Seher-Weiß, S., and von Grünhagen, W., “EC 135 System Identification for Model Following Control and Turbulence Modeling,” *1st CEAS European Air and Space Conference*, Deutsche Gesellschaft für Luft- und Raumfahrt, Bonn, Germany, 2007, Paper 275, pp. 2439–2447.
- [72] Seher-Weiss, S., and von Grünhagen, W., “Comparing Explicit and Implicit Modeling of Rotor Flapping Dynamics for the EC 135,” *CEAS Aeronautical Journal*, Vol. 5, No. 3, 2014, pp. 319–332.
<https://doi.org/10.1007/s13272-014-0109-0>
- [73] Ivler, C. M., “Development and Comparison of Explicit and Implicit Rotor-State Feedback Control Systems for a Fly-by-Wire UH-60,” *American Helicopter Society Rotorcraft Handling Qualities Specialists’ Meeting*, American Helicopter Soc., 2014, Paper 3.
- [74] Seher-Weiß, S., Greiser, S., Wartmann, J., Myrand-Lapierre, V., Gubbels, A., Ricciardi, J., and Hui, K., “Bell 412 System Identification: Comparing Methods and Tools,” *VFS 75th Annual Forum & Technology Display*, Vertical Flight Soc., Philadelphia, PA, 2019, Paper 219.
- [75] Seher-Weiß, S., Tischler, M. B., Scepanovic, P., and Gubbels, A., “Bell 412 System Identification and Model Fidelity Assessment for Hover and Forward Flight,” *Journal of the American Helicopter Society*, Vol. 66, No. 1, 2021, pp. 1–13.
<https://doi.org/10.4050/JAHS.66.012004>
- [76] Seher-Weiss, S., “Comparing Different Approaches for Modeling the Vertical Motion of the EC 135,” *CEAS Aeronautical Journal*, Vol. 6, No. 3, 2015, pp. 395–406.
<https://doi.org/10.1007/s13272-015-0150-7>
- [77] Seher-Weiß, S., “ACT/FHS System Identification Including Rotor and Engine Dynamics,” *Journal of the American Helicopter Society*, Vol. 64, No. 2, 2019, pp. 1–12.
<https://doi.org/10.4050/JAHS.64.022003>
- [78] Schmidt, D. K., *Modern Flight Dynamics*, McGraw-Hill, New York, 2010.
- [79] Seher-Weiß, S., “First Attempts to Account for Flexible Modes in ACT/FHS System Identification,” *43rd European Rotorcraft Forum*, Milano, Italy, 2017, Paper 576, <http://hdl.handle.net/20.500.11881/3818> [retrieved 26 March 2023].
- [80] Wartmann, J., and Seher-Weiss, S., “Application of the Predictor-Based Subspace Identification Method to Rotorcraft System Identification,” *39th European Rotorcraft Forum*, Moscow, Russia, 2013, Paper 7, <http://hdl.handle.net/20.500.11881/546> [retrieved 26 March 2023].
- [81] Wartmann, J., Döring, F. A., and Seher-Weiß, S., “Estimation of Rotor Mast Moments Using a Data-Driven Observer Tuning,” *47th European Rotorcraft Forum*, Virtual, United Kingdom, 2021, Paper 40.
- [82] Anon., *Defence Standard 00-970, Design and Airworthiness Requirements for Service Aircraft*, Part 7—Rotorcraft, Section 9, Ministry of Defence, Glasgow, Scotland, U.K., 2010.
- [83] Greiser, S., and Seher-Weiss, S., “A Contribution to the Development of a Full Flight Envelope Quasi-Nonlinear Helicopter Simulation,” *CEAS Aeronautical Journal*, Vol. 5, No. 1, 2014, pp. 53–66.
<https://doi.org/10.1007/s13272-013-0090-z>
- [84] Greiser, S., and von Grünhagen, W., “Improving System Identification Results Combining a Physics-Based Stitched Model with Transfer Function Models Obtained Through Inverse Simulation,” *AHS 72nd Annual Forum*, American Helicopter Soc. Paper 159, West Palm Beach, FL, 2016.
- [85] Pruter, I., and Duda, H., “A New Flight Training Device for Modern Lightweight Gyroplanes,” *AIAA Modeling and Simulation Technologies Conference*, AIAA Paper 2011-6497, 2012.
<https://doi.org/10.2514/6.2011-6497>
- [86] Duda, H., Sachs, F., Seewald, J., and Lorenz, S., “Dynamic Rollover of Gyroplanes During Landing—Cause and Prevention,” *CEAS Aeronautical Journal*, Vol. 13, No. 2, 2022, pp. 521–533.
<https://doi.org/10.1007/s13272-022-00575-5>
- [87] Doherr, K.-F., and Jann, T., “Test Vehicle ALEX-I for Low-Cost Autonomous Parafoil Landing Experiments,” *14th Aerodynamic Decelerator Systems Technology Conference*, AIAA Paper 1997-1543, 1997.
<https://doi.org/10.2514/6.1997-1543>
- [88] Jann, T., and Doherr, K.-F., “Experimental System ALEX for Autonomous Parafoil Precision Landing of Space Capsules,” *Proceedings of the European Telemetry Conference*, Arbeitskreis Telemetrie e.V., Garmisch-Partenkirchen, Germany, 1998, pp. 282–286.
- [89] Jann, T., Doherr, K.-F., and Gockel, W., “Parafoil Test Vehicle ALEX—Further Development and Flight Test Results,” *15th Aerodynamic Decelerator Systems Technology Conference*, AIAA Paper 1999-1751, 1999.
<https://doi.org/10.2514/6.1999-1751>
- [90] Jann, T., “Development and Flight Testing of an Autonomous Parafoil-Load System Demonstrator,” *25th International Congress of the Aeronautical Sciences*, International Council of the Aeronautical Sciences, Hamburg, Germany, 2006, Paper 504, https://www.icas.org/ICAS_ARCHIVE/ICAS2006/PAPERS/504.PDF [retrieved 26 March 2023].
- [91] Jann, T., and Strickert, G., “System Identification of a Parafoil Load Vehicle—Lessons Learned,” *18th Aerodynamic Decelerator Systems Technology Conference*, AIAA Paper 2005-1663, 2005.
<https://doi.org/10.2514/6.2005-1663>
- [92] Jann, T., “Aerodynamic Model Identification and GNC-Design for the Parafoil-Load System ALEX,” *16th Aerodynamic Decelerator Systems Technology Conference*, AIAA Paper 2001-2015, 2001.
<https://doi.org/10.2514/6.2001-2015>
- [93] Jann, T., “Validation of a Gliding Parachute Simulation Model Through System Identification,” *RTO AVT-133 Specialists Meeting*

- on Fluid Dynamics of Personnel and Equipment Precision Delivery from Military Platforms*, NATO Research and Technology Agency (RTA), Vilnius, Lithuania, 2006.
- [94] Jann, T., "Aerodynamic Coefficients for a Parafoil Wing with Arc Anhedral—Theoretical and Experimental Results," *17th Aerodynamic Decelerator Systems Technology Conference*, AIAA Paper 2003-2106, 2003.
<https://doi.org/10.2514/6.2003-2106>
- [95] Strickert, G., "Study on the Relative Motion of Parafoil-Load-Systems," *Aerospace Science and Technology*, Vol. 8, No. 6, 2004, pp. 479–488.
<https://doi.org/10.1016/j.ast.2004.04.003>
- [96] Strickert, G., and Jann, T., "Determination of the Relative Motion Between Parafoil Canopy and Load Using Advanced Video-Image Processing Techniques," *15th Aerodynamic Decelerator Systems Technology Conference*, AIAA Paper 1999-1754, 1999.
<https://doi.org/10.2514/6.1999-1754>
- [97] Yakimenko, O. A., and Jann, T., *Parametrical Identification of Parachute Systems, Precision Aerial Delivery Systems: Modeling, Dynamics and Control*, Vol. 248, AIAA Progress in Astronautics and Aeronautics, AIAA, Reston, VA, 2015.
- [98] Strickert, G., and Witte, L., "Analysis of the Relative Motion in a Parafoil-Load System," *16th Aerodynamic Decelerator Systems Technology Conference*, AIAA Paper 2001-2013, 2001.
<https://doi.org/10.2514/6.2001-2013>
- [99] Baillie, S. W., and Morgan, J. M., "An In-Flight Investigation into the Relationships Among Control Sensitivity, Control Bandwidth and Disturbance Rejection Bandwidth Using a Variable Stability Helicopter," *15th European Rotorcraft Forum*, No 61, Amsterdam, 1989, <http://hdl.handle.net/20.500.11881/2652>.
- [100] Lusardi, J. A., Tischler, M. B., Blanken, C. L., and Labows, S. J., "Empirically Derived Helicopter Response Model and Control System Requirements for Flight in Turbulence," *Journal of the American Helicopter Society*, Vol. 49, No. 3, 2004, pp. 340–349.
<https://doi.org/10.4050/JAHS.49.340>
- [101] Lusardi, J. A., Blanken, C. L., and Tischler, M. B., "Piloted Evaluation of a UH-60 Mixer Equivalent Turbulence Simulation Model," *American Helicopter Soc. International 59th Annual Forum & Technology Display*, American Helicopter Soc. Paper 134, 2003, <https://ntrs.nasa.gov/api/citations/20030069014/downloads/20030069014.pdf> [retrieved 26 March 2023].
- [102] Hess, R. A., "A Simplified and Approximate Technique for Scaling Rotorcraft Control Inputs for Turbulence Modeling," *Journal of the American Helicopter Society*, Vol. 49, No. 3, 2004, pp. 361–366.
<https://doi.org/10.4050/JAHS.49.36>
- [103] Seher-Weiss, S., and von Grünhagen, W., "Development of EC 135 Turbulence Models via System Identification," *Aerospace Science and Technology*, Vol. 23, No. 1, 2012, pp. 43–52.
<https://doi.org/10.1016/j.ast.2011.09.008>
- [104] Lusardi, J. A., von Grünhagen, W., and Seher-Weiss, S., "Parametric Turbulence Modeling for Rotorcraft Applications: Approach, Flight Tests and Verification," *Royal Aeronautical Soc. Conference on Rotorcraft Handling Qualities*, Liverpool, UK, 2008.
- [105] Seher-Weiß, S., and Jones, M., "Control Equivalent Turbulence Input Models for Rotorcraft in Hover and Forward Flight," *Journal of Guidance, Control, and Dynamics*, Vol. 44, No. 8, 2021, pp. 1–8.
<https://doi.org/10.2514/1.G005931>
- [106] Seher-Weiß, S., and Jones, M., "Evaluation of Control Equivalent Turbulence Input (CETI) Models for Hover and Forward Flight," *47th European Rotorcraft Forum*, 2021, Paper 44.
- [107] Fezans, N., Schwitthal, J., and Fischenberg, D., "In-Flight Remote Sensing and Identification of Gusts, Turbulence, and Wake Vortices Using a Doppler LiDAR," *CEAS Aeronautical Journal*, Vol. 8, No. 2, 2017, pp. 313–333.
<https://doi.org/10.1007/s13272-017-0240-9>
- [108] Cavaliere, D., Fezans, N., Kiehn, D., Quero Martin, D., and Vrancken, P., "Gust Load Control Design Challenge Including Lidar Wind Measurements and Based on the Common Research Model," *AIAA SciTech 2022 Forum*, AIAA Paper 2022-1934, 2022.
<https://doi.org/10.2514/6.2022-1934>
- [109] Fezans, N., Joos, H.-D., and Deiler, C., "Gust Load Alleviation for a Long-Range Aircraft with and Without Anticipation," *CEAS Aeronautical Journal*, Vol. 10, No. 4, 2019, pp. 1033–1057.
<https://doi.org/10.1007/s13272-019-00362-9>
- [110] Kiehn, D., Fezans, N., Vrancken, P., and Deiler, C., "Parameter Analysis of a Doppler Lidar Sensor for Gust Detection and Load Alleviation," *International Forum on Aeroelasticity and Structural Dynamics (IFASD)*, IFASD-2022-105, Universidad Carlos III de Madrid, Madrid, Spain, June 2022.
- [111] Fezans, N., Wallace, C., Kiehn, D., Cavaliere, D., and Vrancken, P., "Lidar-Based Gust Load Alleviation—Results Obtained on the Clean Sky 2 Load Alleviation Benchmark," *International Forum on Aeroelasticity and Structural Dynamics (IFASD)*, IFASD-2022-155, Universidad Carlos III de Madrid, Madrid, Spain, June 2022.
- [112] Hahn, K.-U., Fischenberg, D., Niedermeier, D., and Horn, C., "Wake Encounter Flight Control Assistance Based on Forward-Looking Measurement Processing," *AIAA Atmospheric and Space Environments Conference*, AIAA Paper 2010-7680, 2010.
<https://doi.org/10.2514/6.2010-7680>
- [113] Fischenberg, D., U.S. Patent Application for "Flow Determination Method," Docket No. US-9075074-B2, filed 22 July 2010.
- [114] Ehlers, J., Fischenberg, D., and Niedermeier, D., "Wake Impact Alleviation Control Based on Wake Identification," *Journal of Aircraft*, Vol. 52, No. 6, 2015, pp. 2077–2089.
<https://doi.org/10.2514/1.C033157>
- [115] Schwitthal, J., Fezans, N., and Niedermeier, D., "Integration of Wake Impact Alleviation Control System into Control System Architecture of Modern Fly-by-Wire Aircraft," *5th CEAS Conference on Guidance, Navigation and Control (EuroGNC)*, Council of European Aerospace Societies (CEAS), Milano, Italy, 2019, <https://elib.dlr.de/129433/> [retrieved 26 March 2023].
- [116] Schwitthal, J., "Lidar-Based Wake Identification and Impact Alleviation," Ph.D. Dissertation, DLR Inst. Flight Systems, Braunschweig, Germany, 2017, <https://elib.dlr.de/118265/> [retrieved 26 March 2023].
- [117] Ehlers, J., and Fezans, N., "Airborne Doppler LiDAR Sensor Parameter Analysis for Wake Vortex Impact Alleviation Purposes," *Advances in Aerospace Guidance, Navigation and Control, CEAS EuroGNC Conference Paper*, Springer-Verlag, Cham, 2015.
https://doi.org/10.1007/978-3-319-17518-8_25
- [118] Schwitthal, J., and Fezans, N., "Deriving Lidar Sensor Requirements for Use in Wake Impact Alleviation Functions," *AIAA SciTech 2022 Forum*, AIAA Paper 2022-1936, 2022.
<https://doi.org/10.2514/6.2022-1936>